



Polycrystalline diamond aggregates and their role in Earth's deep carbon cycle

Dorrit E. Jacob^{a,*}, Richard A. Stern^b, Janina Czas^{b,1}, Magnus Reutter^c, Sandra Piazzolo^d, Thomas Stachel^b

^a Research School of Earth Sciences, Australian National University, Canberra, 2601 ACT, Australia

^b Earth and Atmospheric Sciences, University of Alberta, Edmonton, AB T6G 2E3, Canada

^c Dept of Geosciences, Johannes Gutenberg University, D-55077 Mainz, Germany

^d School of Earth and Environment, University of Leeds, Leeds LS2 9JT, United Kingdom

ARTICLE INFO

Associate editor: Dmitri Ionov

Keywords:

Nitrogen
Reaction path modelling
Isotopes
Garnet
Clinopyroxene

ABSTRACT

Polycrystalline diamond aggregates (PDAs) are small rocks composed mostly of diamond grains, but often containing also peridotitic, eclogitic and/or websteritic minerals as accessory phases. PDAs are formed rapidly in Earth's mantle, and the diamonds preserve heterogeneity not often seen in monocrystalline diamond. Here, diamond grains from forty-three PDAs from the Venetia diamond mine (RSA) with grain-sizes < 1 mm are presented. They have heterogeneous and complex cathodoluminescence signatures that are best explained by multiple, separate diamond growth episodes from compositionally distinct COH fluids/melts. The diamonds show a large range of nitrogen concentrations (0.5 to 2,891 at. ppm), $\delta^{15}\text{N}$ (−4.3 to + 16.8 ‰) and $\delta^{13}\text{C}$ values (−27.8 to −7.6 ‰). The positive $\delta^{15}\text{N}$ median of + 6.4 ‰ and negative $\delta^{13}\text{C}$ median of −21.2 ‰ indicate derivation of the diamond-forming fluid from organic materials in subducted oceanic crust and lithosphere. Two PDAs have $\delta^{13}\text{C}$ and $\delta^{15}\text{N}$ values typical for Earth's mantle. Thirty-three PDAs contain websteritic garnets, or peridotitic garnets and clinopyroxenes and/or micas. Unradiogenic ϵNd_i values in the garnets (−15.9 to −29.7) and clinopyroxene (−8.3) and $\delta^{18}\text{O}$ values of 6.49 to 8.09 ‰ in websteritic garnets are consistent with an origin from subducted altered oceanic crust and support the findings from N and C systematics in the diamonds. Nitrogen aggregation data for the diamonds range from 25 % to 100 %B and vary by as much as 60 % within some individual PDAs. We explain the geochemical and isotopic heterogeneity of diamonds and silicates as well as the complex cathodoluminescence features with a model of episodic melt/fluid–rock interaction involving a reducing asthenospheric melt in the cratonic roots or the thermal boundary layer. We suggest that large volumes of PDA are formed in the cratonic roots and thermal boundary layer by this mechanism, making them an important reservoir for carbon storage, which is corroborated with their locally high abundance (ca. 20 %) in some kimberlites.

1. Introduction

Polycrystalline diamond aggregates (PDAs) are a species of natural diamond formed in the Earth's mantle brought to the surface by kimberlites (see Jacob and Mikhail, 2022; Moore and Helmstaedt, 2023 for recent reviews). PDAs are small rocks in which diamond is the major rock-forming mineral (Fig. 1). They are several millimetres to centimetres in size and typically have small overall grain-sizes (<1 mm),

although coarse-grained PDAs with diamond grains > 1 mm exist. Non-diamond phases, (silicates, oxides, carbides, metals) are often (but not always) present as accessory phases and intimately intergrown with the diamond grains and/or occur as micro-inclusions in the diamonds indicating a syngenetic relationship with diamond.

Historically, PDAs have several different names, such as boart, fram-site, stewartite or diamondite (Heaney et al., 2005): we refer to them here as polycrystalline diamond aggregates to contrast them with

* Corresponding author.

E-mail addresses: Dorrit.jacob@anu.edu.au (D.E. Jacob), rstern@ualberta.ca (R.A. Stern), Janina.Czas@NRCan-RNCan.gc.ca (J. Czas), S.Piazzolo@leeds.ac.uk (S. Piazzolo), tstachel@ualberta.ca (T. Stachel).

¹ Present address: Geological Survey of Canada, 601 Booth Street, Ottawa, ON K1S 0W2, Canada.

<https://doi.org/10.1016/j.gca.2024.10.021>

Received 19 November 2023; Accepted 21 October 2024

Available online 28 October 2024

0016-7037/© 2024 The Author(s). Published by Elsevier Ltd. This is an open access article under the CC BY license (<http://creativecommons.org/licenses/by/4.0/>).

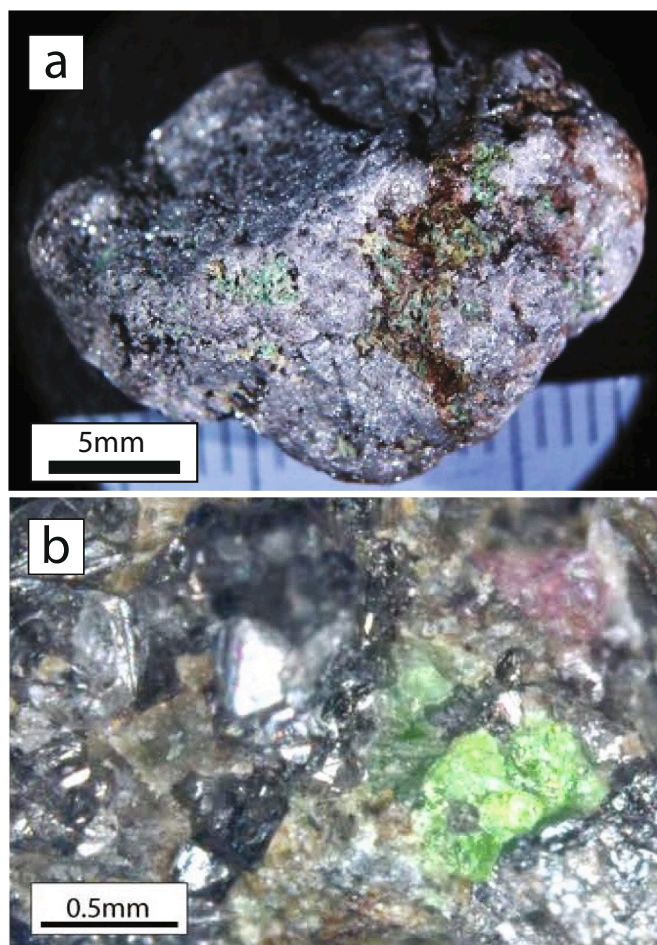


Fig. 1. Photomicrographs of typical polycrystalline diamond aggregates (PDA). Note the dense and fine-grained texture (a) with green clinopyroxene and red garnets intergrown with the diamond crystals (b). (For interpretation of the references to colour in this figure legend, the reader is referred to the web version of this article.)

monocrystalline *gem*-type diamond which we refer to hereafter as ‘monocrystalline diamonds’. PDAs can amount to 20 % of production at some diamond mines. They are reported only from Group I kimberlites (Smith, 1983), namely Jwaneng and Orapa in Botswana (Gurney and Boyd, 1982; Jacob et al., 2011; Kirkley et al., 1995; McCandless et al., 1989), Cullinan (formerly known as Premier) and Venetia in South Africa (Jacob et al., 2000; 2004; 2016) and Mirny, Aikhal, Yubileynaya, Sytykanskaya in Siberia (Kaminsky et al., 1981; Orlov, 1977; Smelova, 1994; Sobolev 1977; Sobolev et al., 2016). A sizeable collection of PDAs at the Natural History Museum in Vienna from an unknown locality is assumed to be from one of the southern African Mines (Kurat and Dobosi, 2000; Dobosi and Kurat, 2002) and is referred to here as the ‘Kalahari’ suite.

Characteristically, PDAs have up to 30 % porosity (Heaney et al., 2005; Jacob et al., 2011) and many of the voids are isolated from the outer surfaces of the rocks (Jacob et al., 2011). Upon crushing, PDAs have released detectable amounts of helium (Gautheron et al., 2005; Mikhail et al., 2019a) or hydrogen (Fourel et al., 2017) and fluid-filled inclusions in diamond of unknown composition have been observed by Transmission Electron microscopy (Jacob et al., 2011). Thus, isolated cavities are not the result of the severe acid cleaning processes which diamonds undergo prior to valuation but indicate the presence of fluids trapped during formation.

The presence of trapped fluid, combined with the overall small grain sizes, are strong indicators for the formation of this diamond species by a

process of heterogeneous nucleation and rapid growth in the presence of fluids oversaturated in carbon (Sunagawa, 2005). Another characteristic of PDAs that stands out globally is that they are commonly compositionally heterogeneous across spatial scales. This manifests at the level of the sample suite at a given locality, for example in carbon isotopes, where significant ranges of over 20 ‰ in $\delta^{13}\text{C}$ have been reported for PDAs from Orapa (Deines et al., 1993; Mikhail et al., 2019b), Jwaneng (Kirkley et al., 1995) and Kalahari (Dobosi and Kurat, 2010). At the scale of individual PDAs, Mikhail et al. (2014a) observed large ranges of $\delta^{15}\text{N}$ values (up to 35 ‰) using a stepped combustion method in a PDA from the Kalahari suite. This heterogeneous picture is reflected by the non-diamond minerals in PDAs, where peridotitic and websteritic garnets (Mikhail et al., 2019b) are found together, or pyrrhotite grains with magnetite rims (Jacob et al., 2011; Jacob et al., 2016) were found in a PDA at Orapa. At within-grain scale, trace element zonation was reported in garnets from PDAs in Venetia (Jacob et al., 2000). Particularly the within-PDA chemical heterogeneity of the diamond grains indicates very localized and short-lived geochemical conditions during growth. Taken together with the small grain sizes and aggregated nature of the diamonds in PDAs these geochemical observations are strong indications for the rapid formation of PDAs, which set them apart from most other diamond species.

We present here detailed characterisation of diamonds and non-diamond minerals from a suite of forty-three PDAs from the Venetia Mine in South Africa (22°26'1"S 29°19'4"E), a mine which is one of the most economically important diamond deposits worldwide (a Tier 1 mine in the classification of Kjarsgaard et al., 2022).

This large coherent dataset for PDAs from the Venetia kimberlite documents the compositional variability of diamond formation conditions even at a single locality. We show that the majority of N and C isotopes in the diamonds are best explained by subducted organic materials contained in the oceanic crust and lithosphere, which is consistent with the elevated $\delta^{18}\text{O}$ and unradiogenic Nd isotopes in the silicates originating from altered oceanic crust subducted into the mantle. A more detailed look at the Venetia PDAs, however, paints a more heterogeneous picture with a subordinate N and C isotopic signature in the sample suite consistent with derivation from Earth’s mantle, higher temperatures than typical for diamond formation, and diamond crystals with low nitrogen aggregation that indicate short mantle residence times and match previous results for recent formation (Jacob et al., 2000). We explain this nuanced picture with a model of episodic metasomatism of the cratonic roots and the thermal boundary layer by small-scale, reducing fluid/melts from the asthenosphere. This model presents a likely major and widespread process for storage and remobilization of deep carbon as diamonds in the cratonic lithosphere and thermal boundary layer. It suggests a significant role for polycrystalline diamond aggregates in the deep carbon cycle.

2. Materials and Methods

2.1. Samples and sample preparation

The sample suite studied here is part of a large collection of PDAs from the Venetia diamond mine in South Africa. The Venetia Mine comprises a cluster of kimberlites that erupted at 520.6 ± 4.6 Ma (weighted average of three ages published by Phillips et al., 1999; Griffin et al., 2014) and is situated in the Proterozoic Limpopo Belt, which represents the collision suture between the Kaapvaal and Zimbabwe cratons within the Kalahari composite craton in southern Africa (Kjarsgaard et al., 2022; Richardson et al., 2009; Seggie et al., 1999). Mantle xenoliths at Venetia are dominantly harzburgites and spinel \pm garnet lherzolites with about 8 % pyroxenites (Hin et al., 2009). They were sampled over a large pressure interval of ca. 2 to 8 GPa, with the pyroxenites at the lower pressure end of this range (Stiefenhofer et al., 1999). Diamonds carried to the surface by the Venetia kimberlite are dominantly peridotitic, with less than 10 % eclogitic and websteritic

parageneses (Viljoen et al., 1999).

We studied forty-three individual PDAs with weights between 1.8 and 70.5 carats (median 10.7 cts). Ten PDAs did not contain visible or fresh silicate minerals, while all other PDAs contained silicates in variable amounts – only a few grains in some PDAs and up to ca. 25 mg in others. We present major and trace element data for silicate minerals in fifteen samples where we found only garnet, five had only clinopyroxene, nine contained both garnet and clinopyroxene, one had garnet plus clinopyroxene and mica, two samples contained garnet and mica, and one contained clinopyroxene and mica (Table S1). Five samples were part of two previously published studies (Jacob et al., 2000, Jacob et al., 2004) and are included here to provide a comprehensive dataset.

Diamond and silicate fragments were recovered by manual crushing of the PDAs and handpicking. All silicate minerals are non-touching. Some PDAs yielded individual grains of silicates only micrometers in size which did not allow preparation for meaningful geochemical analysis with equipment available for this study. Diamond grain sizes were in the range of tens of microns and most often crushing yielded fragments of opaque, tightly fused grains without obvious crystal facets, while clear crystallites were rarely observed. Suitable diamond fragments (individual small clear grains) were used for FTIR analysis while other larger broken fragments of individual PDAs (ca. 100–500 μm in size) were used for SIMS analysis and Electron Backscatter Diffraction (EBSD).

2.2. Analytical Methods

A JEOL JXA 8900 RL microprobe at the Johannes Gutenberg University, Mainz (Germany) was used to determine the major element compositions of garnets, clinopyroxenes and micas using wavelength dispersive analysis and a range of natural and synthetic standards. The data were corrected using the CITZAF procedure (Armstrong, 1995). Detection limits were generally between 0.01 and 0.07 wt% (15 kV, 12 nA, 2 μm beam size).

Trace element concentrations were analysed by Laser Ablation ICPMS at the Johannes Gutenberg University, Mainz (Germany) using an Agilent 7500ce quadrupole ICP-MS coupled with an esi/NWR193 nm wavelength excimer laser following methods described in Jacob (2006). Ablation was carried out at 6.4 J/cm² and 10 Hz, using He as the carrier gas. All measurements were performed on grain mounts using spot size diameters of 100 μm or 60 μm . GLITTER 4.0 software (Griffin et al., 2008) was used for data reduction with NIST SRM 612 (Jochum and Nehring, 2006) as the external standard and ⁴³Ca (for garnet and clinopyroxene) and ²⁹Si (for mica) as the internal standard using values for CaO and SiO₂ from the electron microprobe analyses. USGS glass BCR2-G was measured as an unknown in every session for quality control and always yielded values within 10 % of the published values, except for Zn which was within 20 % of the published value (Table S2). Care was taken to analyse only unaltered and crack-free parts of grains. Time-resolved signals for individual analyses were screened for inclusions or cracks (identified by spikes in the time-resolved signal) and affected parts or complete analyses were discarded accordingly.

Radiogenic Nd isotope work was carried out at the Max-Planck Institute for Chemistry (Cosmochemistry group) following methods published in Jacob et al. (1994). Blanks were 30 pg for Nd and Sm and repeat analyses of the La Jolla reference material (RM) yielded ¹⁴³Nd/¹⁴⁴Nd = 0.51189 (2 σ = 0.00007), in agreement with previously published values.

Sample preparation and secondary ion mass spectrometry (SIMS) were carried out at the Canadian Centre for Isotopic Microanalysis (CCIM), University of Alberta. Fractured pieces of polycrystalline diamond aggregates were organized into three groups and then cast in 25 mm epoxy rounds. These rounds were then ground and polished with conventional equipment using metal-bonded diamond pads on a rotary polisher, then saw-cut and trimmed into mm-square blocks, and assigned mount numbers m1102, m1237, and m1238. These small

epoxy blocks were pressed into regular-size (25 mm) indium mounts M1121, M1243, and M1264 along with diamond and carbon reference materials in order to carry out the isotopic measurements. The mounts were coated with ~ 20 nm of Au prior to scanning electron microscopy (SEM) using a Zeiss EVO MA15 instrument operating at 15 kV and 3–5 nA beam current. Cathodoluminescence images were obtained using a parabolic mirror coupled to a high-sensitivity, broadband photomultiplier detector. An additional 80 nm thickness of Au was added prior to SIMS analysis.

Carbon isotopes (¹³C/¹²C), N abundances, and N-isotopes (¹⁵N/¹⁴N) were determined in separate sessions using the IMS-1280 multi-collector ion microprobe at CCIM using methods and reference materials detailed by Stern et al. (2014) and Palot et al. (2013) with some modifications, as summarized here. Primary beam conditions included the use of 20 keV ¹³³Cs⁺ ions focused to a beam diameter of ~ 10–15 μm . The normal incidence electron gun was not utilized. The primary beam was rastered across a 20 x 20 μm area prior to each analysis for 60–120 s to clean the surface of Au and contaminants and implant Cs. Carbon isotopes were analyzed first, with subsequent N-abundance measurements from the same spot location, followed lastly by a N-isotope measurement adjacent to the previous spot location. Negative secondary ions were extracted through 10 kV potential to the grounded secondary column (Transfer section). Automated tuning of the secondary ions in the Transfer section preceded each analysis.

The analytical setup for C-isotopes included an entrance slit width of 110 μm , field aperture of 5 x 5 mm, a field aperture-to-sample magnification of 100 x, and a fully-open energy slit. Both ¹²C⁻ and ¹³C⁻ were analyzed simultaneously in Faraday cups (L2 using 10¹⁰ Ω amplifier, and FC2 with 10¹¹ Ω) at mass resolutions of ~ 2000 and 2900, respectively. Mean count rates for ¹²C⁻ and ¹³C⁻ were typically 1.0 x 10⁹ and 1.0 x 10⁷ counts/s, respectively, determined over a 75 s counting interval. Total spot-to-spot analysis time (including pre-analysis raster, automated secondary ion tuning, and peak counting) for each measurement was 240 s. The analytical sequence for C-isotopes interspersed measurements of unknowns with the primary diamond RM. For M1121, the primary C-isotope RM was a synthetic HP-HT diamond reference material, S0011B with $\delta^{13}\text{C}_{\text{VPDB}} = -22.58$ ‰. For M1243, the primary C-isotope RM was natural diamond S0270 with $\delta^{13}\text{C}_{\text{VPDB}} = -8.88 \pm 0.10$ ‰. The primary RM was analysed once for every 4 analyses of unknowns. Instrumental mass fractionation (IMF) for ¹³C/¹²C was determined from all the replicate analyses of the diamond RM for the particular analytical session (IP12004, IP13075), where the standard deviation of the ¹³C/¹²C values was ~ 0.06 ‰, following correction for small, systematic within-session changes in IMF. Uncertainties of individual $\delta^{13}\text{C}_{\text{VPDB}}$ analyses propagate within-spot (~0.05 ‰, 1 σ), between-spot (0.05 ‰, 1 σ , blank assigned), and between-session errors (0.01–0.03 ‰, 1 σ), and are typically ± 0.15 ‰ (2 σ).

Nitrogen abundances were determined following C-isotopes. Secondary ion collection conditions included an entrance slit width of 40 μm , field aperture of 3 x 3 mm, and energy slit width of 40 eV transmitting low-energy ions. The molecular ion ratio [¹²C¹⁴N⁻]/[¹²C¹²C⁻] was determined using a Faraday cup–Faraday cup (FC2–L2) combination where ¹²C¹⁴N⁻ > 1 x 10⁵ counts/s, and electron multiplier combination – Faraday cup (EM–L2) where < 1 x 10⁵ counts/s. Mass resolution was ~ 7000 for ²⁶CN⁻ and 2000 for ²⁴C₂ peaks, sufficient to resolve any potential spectral interferences. Electron multiplier counts were corrected for background and deadtime (50 ns). Total spot-to-spot analysis time was 210 s. The sensitivity factor for CN⁻/C²⁻ to calculate N abundance was determined relative of the diamond reference materials S0011G (420 at. ppm) and S0280 (1670 at. ppm, see Stern et al., 2014). A second nitrogen abundance measurement was determined for some spots from the subsequent N-isotope analyses using primary-beam-normalized secondary ion yields of ¹²C¹⁴N⁻ for the diamond RM. Detection limits for N in this study are < 0.1 at. ppm.

Nitrogen isotopes (¹⁵N/¹⁴N) were determined on a subset of spots with > 50 at. ppm N, placed adjacent to the previous C-[N] analyses. The

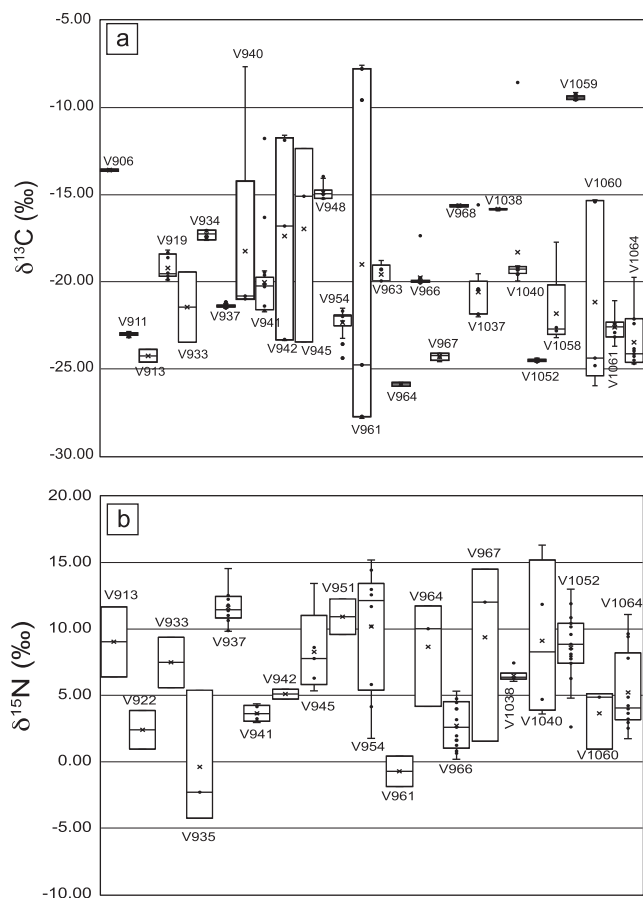


Fig. 2. Box and whisker plots for $\delta^{13}\text{C}$ (a) and $\delta^{15}\text{N}$ (b) data in table S3 for PDAs with more than one SIMS spot measured. For box and whisker plots for nitrogen concentrations see Fig. S1.

$^{12}\text{C}^{14}\text{N}^-$ and $^{12}\text{C}^{15}\text{N}^-$ molecular ions were analyzed simultaneously in a Faraday cup (L'2 using $10^{11} \Omega$ amplifier)-EM combination at mass resolutions of 6800 and 7000, respectively. Mean count rates were for $^{12}\text{C}^{14}\text{N}^-$ ($>3 \times 10^5$ counts/s) and $^{12}\text{C}^{15}\text{N}^-$ were determined over a 375 s (75×5 s blocks) counting period. Faraday cup baseline for N-isotopes was measured prior to each analysis. Electron multiplier counts were corrected for background and deadtime (50 ns). Total spot-to-spot analysis time was 690 s. The analytical sequence interspersed measurements of unknowns with diamond S0270 having $\delta^{15}\text{N}_{\text{AIR}} = -0.40 \pm 0.50$ ‰ in a 4:1 ratio. Instrumental mass fractionation (IMF) was determined from utilizing all the replicate $^{12}\text{C}^{15}\text{N}^-/^{12}\text{C}^{14}\text{N}^-$ analyses of S0270 from two sessions (IP13077, $N = 32$; IP14005, $N = 23$), for which the standard deviation was ± 0.26 ‰ for both. The 95 % confidence uncertainty for $\delta^{15}\text{N}_{\text{AIR}}$ averaged $\sim \pm 0.5$ ‰ for individual analyses of S0270 with $N \sim 2000$ at. ppm. The PDA diamonds with their variable concentrations of N have uncertainties between ± 0.5 ‰ and 3.3 ‰.

Infrared absorption spectra were collected at Macquarie University (GAU) and in the De Beers Laboratory for Diamond Research at the University of Alberta. At GAU, Macquarie University, we used a nitrogen purged Nicolet iN10 microscope, operated via Omnic Pictra software. Using a $100 \times 100 \mu\text{m}$ aperture and a liquid nitrogen-cooled detector, each spectrum was collected over the range of $4000\text{--}675 \text{ cm}^{-1}$ with a resolution of 1 cm^{-1} , by 16 scans in 6 s. At the De Beers Laboratory for Diamond Research, University of Alberta we used a Thermo Fisher Nicolet Nexus 470 FTIR spectrometer (bench) coupled to a Continuum IR microscope with a liquid nitrogen-cooled MCT detector. Spectra were acquired over the range of $4000\text{--}650 \text{ cm}^{-1}$ with a spectral resolution of 4 cm^{-1} . Two hundred scans were averaged, and the spatial resolution was set to $50\text{--}100 \mu\text{m}$ with the aid of a square aperture. Spectra were

first manually corrected for baseline and then normalized to 1 cm path length employing the spectrum of a nitrogen-free (Type II) diamond of 1 cm thickness. The peak area of the hydrogen-related (N_3VH) center at 3107 cm^{-1} was determined on this normalized spectrum, involving a local background correction to first remove all diamond-related absorbance. All spectra were decomposed into spectral components using the CAXBD spreadsheet coded by David Fisher (De Beers Ignite, Maidenhead, UK). Nitrogen concentrations (at. ppm) were then calculated from absorption coefficient values at 1282 cm^{-1} using the factors of Boyd et al. (1994) for A-centers and Boyd et al. (1995) for B-centers. Detection limits and errors depend on sample quality but typically range from 5 to 10 at. ppm and about 5–10 % of the concentration, respectively.

Quantitative crystallographic orientation data were collected using automatically indexed Electron Backscattered Diffraction (EBSD) patterns, acquired with an HKL NordlysNano high sensitivity EBSD detector and indexed using the Aztec analysis software (Oxford instruments). Analysis was performed on a Zeiss IVO SEM (Macquarie University, Sydney) at high vacuum, with an accelerating voltage of 20 kV, a beam current of 8.2 nA and a working distance of 9.5–10.5 mm. The analysed points were derived from a rectangular grid with $2 \mu\text{m}$ step size using a beam scan.

3. Results

3.1. Stable isotopes, cathodoluminescence imaging and Electron Backscatter Diffraction of diamonds

$\delta^{13}\text{C}$ values for individual spots on diamonds measured by ion microprobe (Table S3) range from -27.8 to -7.6 ‰ (Fig. 2a) with averages for individual PDAs ranging from -26.2 to -9.4 ‰.

The median for the entire suite is -21.2 ‰, with no significant difference in distribution between diamonds with different silicate parageneses. This range covers a significant part of the ^{13}C depleted end of the worldwide distribution for inclusion-bearing monocrystalline diamonds (total range: -41.4 ‰ to $+2.5$; Stachel et al., 2022b), and the PDA median of -21.2 ‰ differs distinctly from the medians of peridotitic (-4.9 ‰) and eclogitic (-6.5 ‰) lithospheric monocrystalline diamonds (Stachel et al., 2022b). Strongly negative values in the worldwide database are typically associated with eclogitic monocrystalline diamonds (extending to -40.7 ‰; Stachel et al., 2022b) and a similar range of negative values have been measured in monocrystalline diamonds with websteritic paragenesis (Stachel et al., 2022b). Graphite pseudomorphs after websteritic diamond at Beni Bousera (Morocco) range from -27.6 to -16.4 ‰ and have a median of -21.0 ‰ (Stachel et al., 2022b).

Nitrogen concentrations cover a range from 0.5 to 2,891 at. ppm (Fig. S1). This range coincides with the range of monocrystalline diamonds (typically up to 1,500 at. ppm but outliers up to 5,004 at. ppm are observed; Smart et al., 2011). $\delta^{15}\text{N}$ values for individual SIMS spot analyses range between -4.3 and $+16.8$ ‰ (Fig. 2b) with a median for the entire suite of $+6.4$ ‰ (Table S3). No correlation with silicate paragenesis was observed. This $\delta^{15}\text{N}$ range is within the very large range of -39.4 to $+16.9$ ‰ for monocrystalline diamonds (Stachel et al., 2022b and references therein), but the median for the PDAs is significantly shifted to a positive value ($+6.4$ ‰) compared to the negative median for monocrystalline diamonds (-2.1 ‰; Stachel et al., 2022b and references therein). Some Venetia PDAs show considerable heterogeneity in $\delta^{15}\text{N}$ values within individual diamond grains (Fig. 2b) and also in N concentration (Fig. S1 a, b), some spanning a significant portion of the PDA suite's total range. The PDAs generally do not show covariations between $\delta^{13}\text{C}$, $\delta^{15}\text{N}$ and nitrogen concentrations.

The intensity of diamond cathodoluminescence (CL) can be related to differences in the concentration of various atomic defects, many of which involve nitrogen in the diamond lattice (Vasilev et al., 2021 and references therein). Thus, CL images can highlight growth zonation (Smart et al., 2011) and deformation (Gaillou et al., 2012). In this

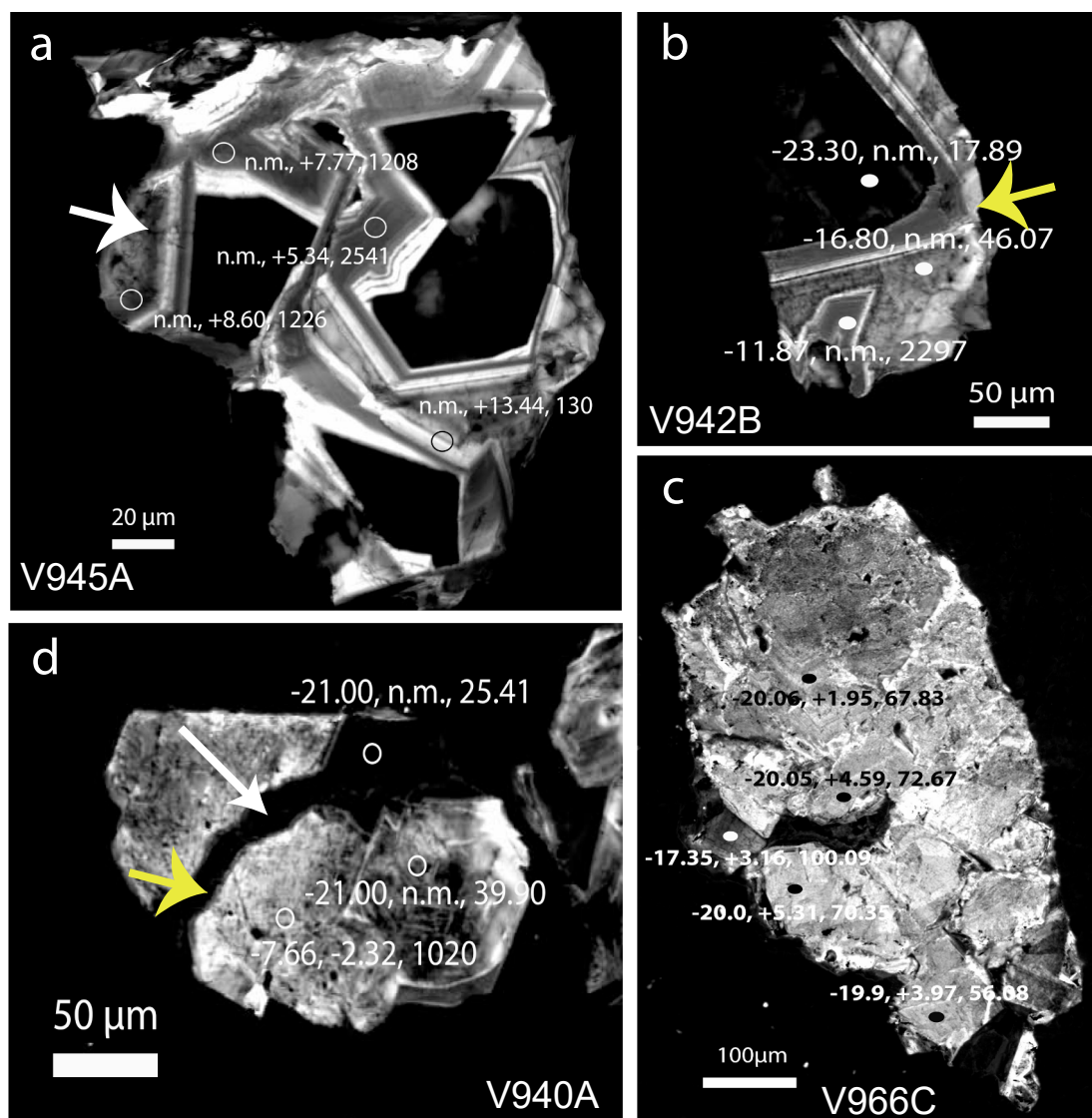


Fig. 3. CL images showing representative features in fragments of PDAs analysed for $\delta^{13}\text{C}$, $\delta^{15}\text{N}$ and nitrogen concentrations by SIMS. Locality of SIMS spots (not to scale) and data displayed as $\delta^{13}\text{C}$ (‰), $\delta^{15}\text{N}$ (‰), N (at.ppm). n.m. = not measured. White arrow in (a) points to growth layers, short yellow arrows in (b) and (d) point to rounded edges and embayed grain boundaries that indicate resorption. Long white arrow in (d) points to a diamond veinlet separating aggregated crystallites of diamond. For Scanning Electron Microscopy images of these fragments see Fig. S2, for individual results and analytical uncertainties see Table S3. (For interpretation of the references to colour in this figure legend, the reader is referred to the web version of this article.)

sample suite, CL intensity roughly correlates with the total concentration of nitrogen measured by SIMS, with low CL intensity areas having low nitrogen abundances and high CL intensity areas being enriched in nitrogen (e.g. Fig. 3). Typically, the PDA fragments studied by SEM and SIMS are a few hundred μm in size and Scanning Electron Images (SEI) depict them as homogeneous fractured pieces of diamond without apparent crystal faces (Fig. S3). However, in CL most pieces are heterogeneous: Many diamond fragments show angular layers of different CL intensity interpreted as growth zonation (e.g. Fig. 3a, white arrow), embayments and rounded edges are signs of resorption (Fig. 3b, d, yellow arrows), while a minor part of the studied PDA fragments are homogeneous in CL (Fig. 3c). One fragment consisting only of diamond (Fig. 3d) comprises several aggregated crystallites in CL (Fig. 3d), each ca. 80 μm in size, some with rounded grain boundaries, which are separated by a diamond vein with very dark CL greyscale (white arrow in Fig. 3d). This is similar to textures described in diamonds from eclogite xenoliths from the Fort a la Corne kimberlite, Sask craton (Czas et al., 2018).

Our EBSD results show that diamond growth layers defined by

different CL greyscales are transected by grain boundaries (Fig. 4) rather than coincide with them. This indicates that current grain boundaries and CL growth stages have developed at different times, i.e. grain boundaries must have moved after diamond growth documented by CL signatures. Our EBSD data also shows that crystal orientation of the diamond grains is near-random (Fig. S4), which agrees with formation by rapid, heterogeneous nucleation and crystal growth (e.g. Davey and Garside, 2000) with a lack of significant subsequent crystal plastic deformation. This differs from Kalahari PDAs, where EBSD shows that they experienced plastic deformation (Rubanova et al., 2012).

3.2. IR-spectroscopy of diamond grains

Nitrogen abundances in the twenty-one PDAs measured by FTIR spectroscopy span a wide range from 0 to 1,670 at. ppm (Table 1). This range is smaller than the range recorded by SIMS (see above), likely because different populations of grains were measured with FTIR and with SIMS and much larger analytical volumes are captured in FTIR analyses ($\sim 100 \mu\text{m}$) compared to SIMS (where a pit of $\sim 15 \times 15 \times 1 \mu\text{m}$

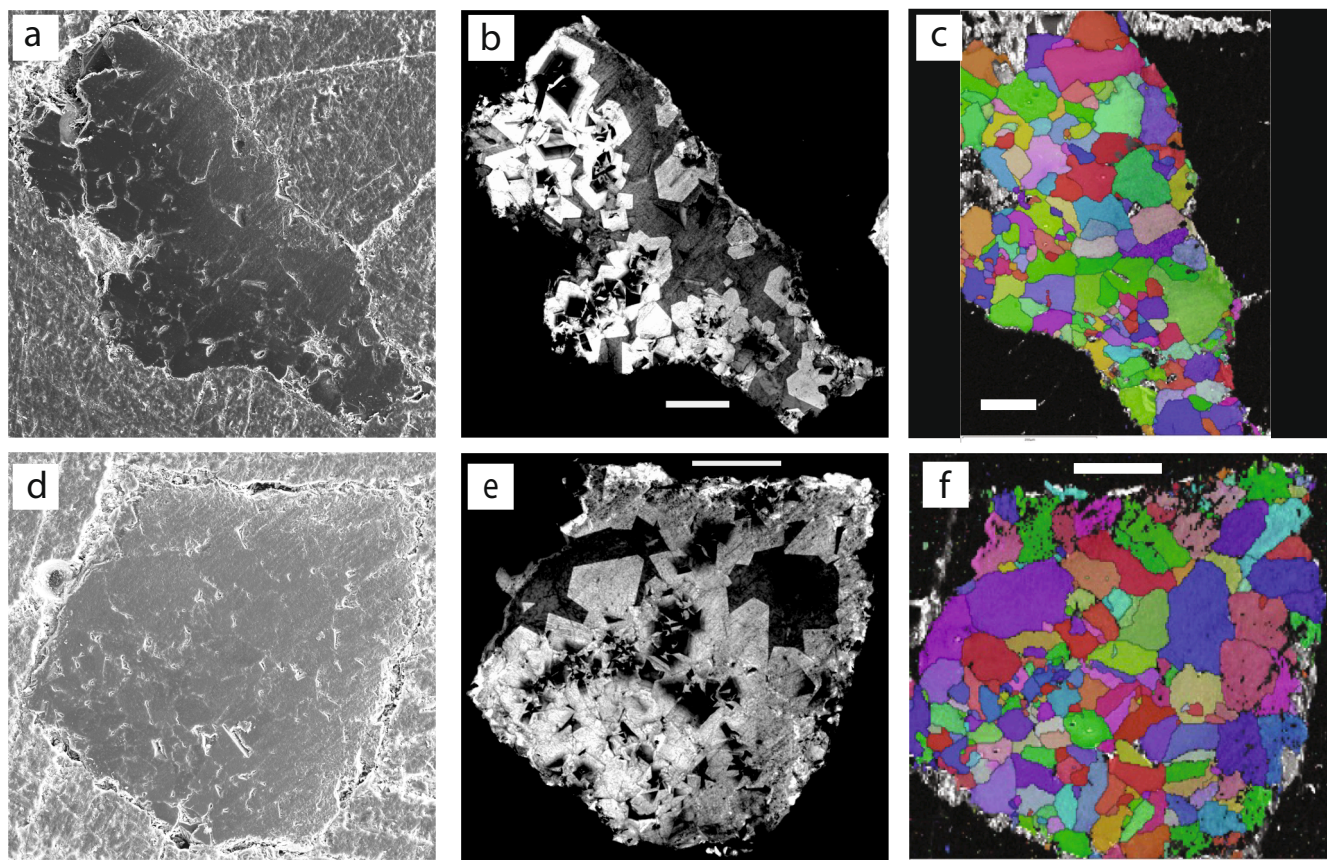


Fig. 4. Scanning Electron Microscopy images (a, d), Backscatter Electron images of CL features (b, e) and crystallographic orientation (c, f) of diamond in the PDAs derived by Electron Backscatter Diffraction analysis. Sample V1064A is shown in panels a-c, V1064B in panels d-f. Different colours in c and f indicate different crystallographic orientation, black lines are grain boundaries defined by $> 10^\circ$ misorientation. Scale bars are 100 μm .

is sputtered from the sample surface). Several PDAs in which more than one diamond grain was analysed are heterogeneous in N content and some of them vary by several 100 at. ppm, which agrees with nitrogen concentration results by SIMS (Table 1). Nitrogen aggregation states, expressed as the $\%B = [100B/(A + B)]$ (relative proportion of nitrogen in fully aggregated B centers; Evans and Qi, 1982), range from 0 % to 100 % (median 75 %) and the majority of diamond grains have highly aggregated nitrogen (Fig. 5a). Notably, nitrogen aggregation states in some individual PDAs, such as V1038 and V925, are heterogeneous (Table 1). Most analysed samples contain IR-active hydrogen in the form of N_3VH defects (Goss et al., 2014) evidenced by the common presence of an absorption band at 3107 cm^{-1} with intensities (measured as peak area) up to 113 cm^{-2} (Table 1). Calculated temperatures for an assumed mantle residence time of 1 Ga (Taylor et al., 1996) show a distribution (Fig. 5b) skewed to higher temperatures than for Southern African monocrystalline diamonds (Fig. 5c), suggesting that the Venetia PDAs originate from deeper in the mantle than the monocrystalline diamonds assuming an identical mantle residence time of 1 Ga (see Discussion).

3.3. Major element geochemistry of silicates intergrown with the diamonds

Garnets in Venetia PDAs are pyrope-almandine-grossular solid solutions characterised by moderate to low CaO and a range of Cr_2O_3 contents (Fig. 6a) as well as variable Mg# (molar $\text{Mg}\# = [\text{Mg}/(\text{Mg} + \text{Fe})] \times 100 = 59.2$ to 84.8; Fig. 6b). Using Grütter et al.'s. (2004) classification instead, the majority are G9 (lherzolitic) or G4 (low-Ca eclogitic/pyroxenitic), with one (V1015) in the G12 field (wehrlite – Table 2a, Table 2b, Fig. 6a). Websteritic garnets are, however, somewhat ill-defined in this scheme and show overlaps with the eclogite and

megacryst fields. Using the alternative classification method of Sobolev et al. (1973), the suite of G4 garnets can be classified as low-Cr websteritic, and the G9 as high-Cr peridotitic. G12 garnets are not classified in this scheme. We refer to the Venetia PDA garnets as peridotitic, wehrlitic and websteritic here, noting that an earlier publication on four PDAs from this suite classified these as (low Ca) eclogitic (Jacob et al., 2000). These are re-classified here as websteritic for coherence. The garnet compositions are within the range for PDAs from Mirny (Sobolev et al., 2016), Orapa (Mikhail et al., 2019b) and the Kalahari suite (Dobosi and Kurat, 2002).

Clinopyroxenes are diopsides, augites or omphacites and span a large range of molar Cr# ($\text{Cr}/(\text{Cr} + \text{Al}) \times 100$) from 1 to 57. The majority has high Cr# while only two (V947, V961) are low (Fig. 6b). The classification scheme of Aulbach et al. (2002) defines peridotitic clinopyroxenes as having $\text{Mg}\# > 85$, $\text{Cr}\# > 10$, and $< 2\text{ wt}\% \text{ Na}_2\text{O}$. The two low-Cr# clinopyroxenes are pyroxenitic-eclogitic using the Aulbach et al. (2002) method, while the high Cr clinopyroxenes have Mg- and Cr-# typical for peridotitic clinopyroxenes, although most have Na_2O concentrations that exceed the cut-off of 2 wt% of Aulbach et al. (2002) (Table 3). However, the Na_2O cut-off of $< 2\text{ wt}\%$ is not entirely robust; for example, 14 % of lherzolitic clinopyroxenes in the database of Stachel et al. (2022a) have $\geq 2\text{ wt}\% \text{ Na}_2\text{O}$. Based on their relatively low jadeite component, the two pyroxenitic-eclogitic clinopyroxenes are websteritic. Where garnets and clinopyroxenes coexist in the same sample, both minerals classify as the same paragenesis (Table S1), except for PDA V1015 where a wehrlitic garnet occurs with peridotitic cpx in non-touching paragenesis.

Mica in PDA V940 coexists with websteritic garnet (Table S1). The mica has a high TiO_2 content (3.03 wt%), and its low Mg# of 80.9 and low Cr_2O_3 content (0.13 wt%) are consistent with a websteritic

Table 1

FTIR data for Venetia PDAs. 'UA' samples were measured at the University of Alberta, all others were measured at Macquarie University.

sample	para	IB' (cm ⁻¹)	N total (ppm)	% IaB	H @ 3107 cm ⁻¹	Platelet position (cm ⁻¹)	T [N,3Ga]	T [N,1Ga]	T [N,0.5 Ga]	T [N,0.1 Ga]
V913-1	p	400	540	74.1	11	1365	1153	1181	1199	1243
V913-2	p	250	370	67.6	15	1365	1154	1182	1201	1245
V913-6	p	240	340	71.0	12	1362	1160	1189	1207	1252
V933-3	p	270	380	71.0	14	1362	1158	1186	1204	1249
V933-7	p	330	460	72.0	10	1362	1154	1182	1200	1245
V933-9	p	300	430	70.0	13	1362	1153	1181	1199	1244
V935-1	p	275	431	64.0			1146	1174	1192	1236
V935-2	p	414	624	66.0			1140	1167	1185	1229
V935-4	p	348	531	66.0			1143	1171	1189	1233
V935-6	p	307	506	61.0			1139	1167	1185	1228
V935-7	p	386	587	66.0			1141	1168	1186	1230
V935-8	p	391	550	71.0			1148	1176	1194	1238
V935-UA1	p	275	431	63.8			1146	1174	1192	1236
V935-UA2	p	414	624	66.4			1140	1167	1185	1229
V935-UA4	p	348	531	65.7			1143	1171	1189	1233
V935-UA6	p	307	506	60.8			1139	1167	1185	1228
V935-UA7	p	386	587	65.8			1141	1168	1186	1230
V951	p	422	570	74.0	22	1363	1151	1179	1198	1242
V962-3	p	99	140	71.0	2	1379	1183	1213	1232	1278
V962-5	p	0	0	0.0	0					
V962-6	p	20	20	99.5	2	1367	1370	1408	1432	1492
V964-3	p	281	370	76.0	15	1365	1165	1193	1212	1257
V964-4	p	260	380	68.4	15	1365	1155	1183	1201	1245
V964-5	p	260	400	65.0	13	1365	1149	1177	1196	1240
V965-1	p	279	300	93.0	6	1362	1208	1238	1258	1306
V965-2	p	291	310	94.0	5	1365	1212	1242	1262	1310
V965-3	p	230	250	92.0	7	1362	1209	1239	1259	1307
V965-4	p	130	130	99.5	4	1379	1310	1345	1368	1423
V965-7	p	70	70	99.5	3	1371	1330	1365	1389	1445
V965-9	p	370	370	99.5	6	1367	1279	1312	1334	1387
V967-1	p	309	490	63.0	8	1365	1142	1170	1188	1231
V967-3	p	350	530	66.0	4	1365	1144	1171	1189	1233
V967-4	p	497	720	69.0	13	1365	1139	1167	1185	1228
V967-5	p	381	560	68.0	3	1365	1144	1172	1190	1234
V967-6	p	497	700	71.0	2	1365	1142	1170	1188	1232
V967-7	p	352	510	69.0	3	1365	1148	1176	1194	1238
V967-8	p	281	460	61.0	9	1365	1142	1169	1187	1231
V967-9	p	449	670	67.0	8	1365	1139	1166	1184	1228
V967UA3	p	476	665	71.5			1144	1172	1190	1234
V967UA5	p	354	568	62.4			1138	1165	1183	1227
V971UA2	p	381	495	77.0			1159	1187	1206	1250
V971UA3	p	606	725	83.6			1160	1188	1207	1251
V971UA4	p	553	662	83.6			1162	1191	1209	1254
V971UA6	p	673	788	85.4			1161	1190	1208	1253
V1015-1	we	230	285	80.7	11	1362	1179	1208	1227	1273
V1015-3	we	229	290	79.0	7		1176	1205	1223	1269
V1015-5	we	230	285	80.7	11	1365	1179	1208	1227	1273
V1015UA11	we	355	421	84.2			1175	1204	1223	1269
V1015UA9	we	345	404	85.4			1178	1207	1226	1272
V954-2	n/a	240	265	90.6	15	1363	1203	1233	1252	1300
V954-4	n/a	190	240	79.0	16	1362	1180	1210	1229	1275
V954-7	n/a	260	300	86.7	15	1362	1189	1218	1238	1284
V1038-1	n/a	0	30	1.0	1	1377	1087	1112	1129	1169
V1038-2	n/a	80	160	50.0	2	1365	1157	1185	1204	1248
V1038-3	n/a	0	30	1.0	2	1369	1087	1112	1129	1169
V1038-4	n/a	0	30	1.0	2	1379	1087	1112	1129	1169
V1038UA2	n/a	78	146	53.2			1163	1191	1210	1254
V1040-1	n/a	290	380	76.3	6	1365	1165	1193	1212	1257
V1040-5	n/a	372	490	76.0	10	1365	1158	1186	1204	1249
V1040-6	n/a	200	260	76.9	6	1365	1175	1204	1223	1269
V1052-1	n/a	70	70	99.5	3		1330	1365	1389	1445
V1052-1	n/a	71	71	99.5	2		1329	1365	1388	1445
V1052-5	n/a	100	100	99.5	3		1319	1354	1376	1432
V1064-1	n/a	300	380	78.9	16	1362	1168	1197	1216	1261
V1064-3	n/a	260	340	76.5	13	1362	1168	1196	1215	1260
V1064-5	n/a	221	320	69.0	16	1362	1160	1188	1206	1251
V911*	w	10	10	99.5	0		1394	1432	1457	1519
V925-1*	w	0	0	0.0			1357			
V925-6*	w	30	30	99.5				1394	1418	1477
V925-7*	w	0	0	0.0			1147			
V940	w	20	80	25.0	1		1175	1175	1193	1237
V942-2	w	200	260	77.0	5	1367	1161	1204	1223	1269
V942-6	w	997	1120	89.0	7	1369	1153	1189	1207	1252
V942-7	w	1503	1670	90.0	16	1367	1153	1181	1200	1244

(continued on next page)

Table 1 (continued)

sample	para	IB' (cm ⁻¹)	N total (ppm)	% IaB	H @ 3107 cm ⁻¹	Platelet position (cm ⁻¹)	T [N,3Ga]	T [N,1Ga]	T [N,0.5 Ga]	T [N,0.1 Ga]
V942-8(1)	w	1206	1370	88.0	6	1369	1189	1181	1199	1244
V942-8(2)	w	428	470	91.0	9	1369	1151	1218	1237	1284
V942UA6	w	883	1056	83.7			1158	1178	1197	1241
V942UA7	w	1455	1598	91.1			1155	1186	1204	1249
V942UA8	w	1199	1352	88.7			1	1183	1202	1246
V945	w	10	20	50.0		1375		1211	1242	1262
V968-1	w	10	20	50.0	1		1211	1242	1262	1310
V968-7	w	10	15	66.7	1		1238	1270	1291	1341

IB' is the integrated absorption of the platelet peak; # area (in cm⁻²) under the hydrogen-related (N₃VH) peak at 3107 cm⁻¹; p = peridotitic, w = websteritic, we = wehrlitic, n/a = not available, * Jacob et al. (2000).

paragenesis (Shu et al., 2024). Micas in three other PDAs (V933, V1054, V1060) are peridotitic with Mg# of 90 or above (Table 4), Cr₂O₃ concentrations of 0.43–1.5 wt% and similar or lower TiO₂ contents to V933 mica. These micas occur in the PDAs only as a couple of grains, as the only mineral (V1054), coexisting with peridotitic garnet (V933) or with peridotitic garnet and clinopyroxene (V1060).

3.4. Trace elements and radiogenic isotopes in the silicates

Chondrite-normalized Rare Earth Element (REE_N) patterns (Fig. 7) for the peridotitic/wehrlitic garnets are depleted in Light REE (LREE) with relatively flat to slightly sinusoidal Heavy REE (HREE), with most having Lu/Sm < 0.4. V971 garnet has the highest Lu/Sm of 1.8. In comparison, websteritic garnets have positively sloped, convex-upward REE_N patterns with Lu/Sm > 1 and high HREE abundances (up to ca. 50 times chondritic). Clinopyroxenes have humped REE_N patterns that peak at Nd (~20–80x chondritic) and then decrease to near chondritic HREE abundances (e.g. Lu is 0.44 to 2 times chondritic). Neither garnet nor cpx exhibit Eu-anomalies. Primitive Mantle normalized Zr/Hf ratios in websteritic garnets have a small range of 1.1 to 1.5 despite a ca. 5-fold variation in Zr and Hf concentrations (Fig. 8a). Peridotitic garnets show a larger variation of Zr/Hf ratios between 1.0 and 2.2, trending negatively with Yb/Sm ratios (Fig. 8a). The wehrlitic garnet in V1015 has trace element characteristics reminiscent of the lherzolitic group (Fig. 7b, 8a, S5a). Clinopyroxenes have variable High Field Strength Element (HFSE) concentrations and Primitive Mantle normalized Zr/Hf ratios vary between 0.4 and 1.2 (not shown).

Websteritic and peridotitic garnets are distinguished in a plot of Sc/Zn versus Cr concentrations (Fig. 8b), consistent with the classification based on their major element compositions. Zn is typically hosted in olivine at high pressures (as opposed to spinel at lower pressures), hence high Sc/Zn together with high Cr concentrations are consistent with equilibration with olivine, although olivine was not observed in the PDAs. Wehrlitic garnet V1015 is associated with the peridotitic group (Fig. 8b).

Peridotitic garnets (V913, V968) and peridotitic clinopyroxene (V968) from two PDAs could be handpicked at quantities that allowed analysis of Nd isotopes, yielding very unradiogenic ¹⁴³Nd/¹⁴⁴Nd ratios with initial ε_{Nd}-values of -30 and -26 for the garnets and -8.5 for the clinopyroxene (Fig. 9, Table 5). The garnet values are even more negative than those published previously for websteritic garnets in this Venetia suite of -15.9 to -21.7 (Jacob et al., 2000, Table 5). Collectively, they lie to the unradiogenic end of the range measured for individual peridotitic diamond inclusions at Venetia (-62 to +157; Koornneef et al., 2017).

Micas differ significantly in their trace element compositions between different PDAs (Table 3). Comparison with micas found in South African mantle xenoliths (Erlank et al., 1987; Dawson and Smith, 1975; 1977; Delaney et al., 1980; Giuliani et al., 2013; Giuliani et al., 2014, 2016; Grégoire et al., 2002; Jacob et al., 2009; Jones et al., 1982; Matson et al., 1986; Rehfeldt et al., 2008; Rosenbaum 1993) and Ti- and Cr-rich phlogopites in kimberlites (Giuliani et al., 2016; Delaney et al., 1980) reveals a dichotomy: in a plot of Ti vs Ni (Fig. 8c), two of the micas plot

with those from xenoliths, while the other two plot closer to kimberlitic micas. For the Ti-rich micas this suggests a genetic relationship to metasomatism by kimberlite magma, perhaps prior to or during ascent to the surface.

3.5. Trace element heterogeneity

In situ trace element analyses show intra-grain variability for the first-row transition elements, such as Ni, Cr, V and Zn, and also for High Field Strength Elements (HFSE) in silicate minerals in five PDAs that significantly exceed the analytical external reproducibility. For example, Ni -contents in V906 garnet vary between 4.8 to 102 ppm (Jacob et al., 2004), and in V948 by a factor of 2. Zr/Hf ratios in V948 also vary by a factor of ca. 2 (see Fig. 11 in Jacob and Mikhail, 2022). All five PDAs listed here have been part of published studies in which trace element heterogeneity has been addressed in detail. Jacob et al. (2004) attributed the heterogeneity in garnet Ni-content to partitioning of a proportion of the Ni into syngenetic Fe-metal in V906. The heterogeneity in HFSE in V911, V919, V925 and V948 were used by Jacob et al. (2000) to argue for a young formation age for these four PDAs, based on estimates for typical diffusion timescales.

4. Discussion

Overall, our results show that the majority of PDAs at Venetia have highly aggregated nitrogen with δ¹⁵N and δ¹³C values of the diamonds indicating derivation from subducted oceanic crustal and lithospheric carbon and nitrogen. This is corroborated by δ¹⁸O and ε_{Nd} values of the silicates, which agree with the origin of the diamond fluids from subducted ancient oceanic crust. While these geochemical and isotopic signals suggest a lithospheric origin for the PDAs, individual PDAs from this suite have a deeper origin as suggested by metallic inclusions requiring higher formation temperatures (see below and Jacob et al. 2004). This corroborates evidence from a PDA from Orapa for a deep of origin from 320–330 km (Jacob et al., 2016) and suggests that processes leading to formation of PDAs in the mantle are more complex.

The most striking characteristics of the Venetia PDAs are the prevalence of websteritic garnets, which otherwise occur only as very rare inclusions in monocrystalline diamonds, and their geochemical and isotopic heterogeneity, which they share with PDAs worldwide (Jacob and Mikhail 2022). For example, while most diamonds in the Venetia PDAs plot in the field for subducted oceanic crustal organic material (Fig. 10), some PDAs show a distinct N and C isotopic mantle signal. Similarly, despite having mainly highly aggregated nitrogen, some diamond grains in the Venetia PDAs have low degrees of nitrogen aggregation (Fig. 5a) and therefore short mantle residence times, supporting recent formation ages inferred from trace element heterogeneity in websteritic garnets (Jacob et al. 2000). A conceptual model for the origin and formation of PDAs at Venetia and elsewhere must accommodate this detailed and nuanced evidence. In the following, we will address some of these most significant characteristics of the Venetia PDAs before bringing these together in a conceptual model for the PDAs and their significance for the deep carbon cycle.

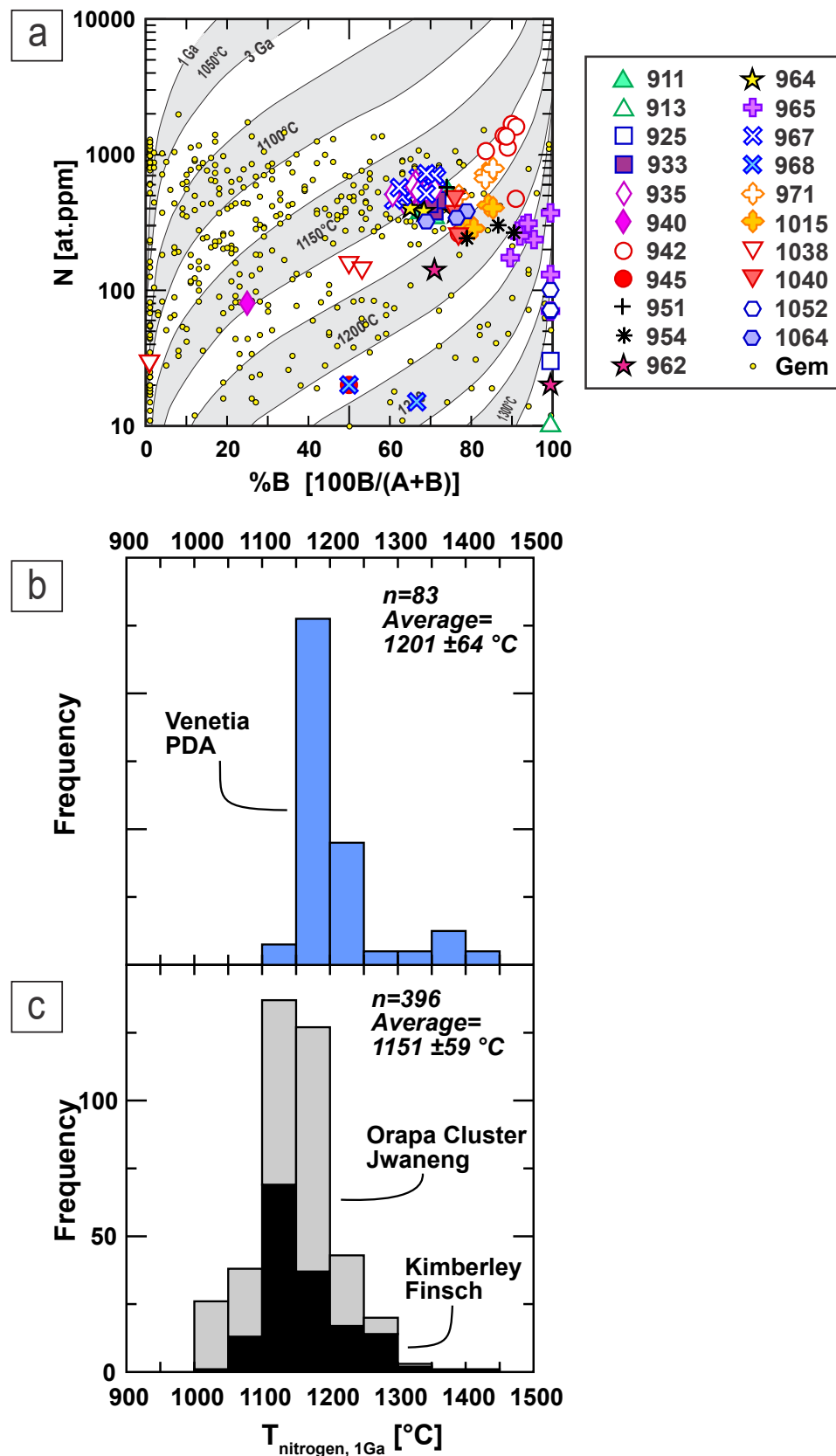


Fig. 5. (a) Nitrogen content (at. ppm) versus nitrogen aggregation (expressed as the relative percentage of nitrogen in fully aggregated B centres, %B). Isotherms are calculated for mantle residence times of 1 and 3 Gyr (calculated after Taylor et al. 1996). Large symbols refer to Venetia PDAs from this study, small yellow dots represent inclusion-bearing gem diamonds from worldwide sources (Stachel et al., 2022b). (b) Nitrogen-based temperature estimates (calculated after Taylor et al. 1996) for PDAs from Venetia and (c) from gem diamonds from the Kalahari Craton (Orapa cluster and Jwaneng, Botswana, in grey and Finsch and Kimberley [De Beers Pool], South Africa, in black). (For interpretation of the references to colour in this figure legend, the reader is referred to the web version of this article.)

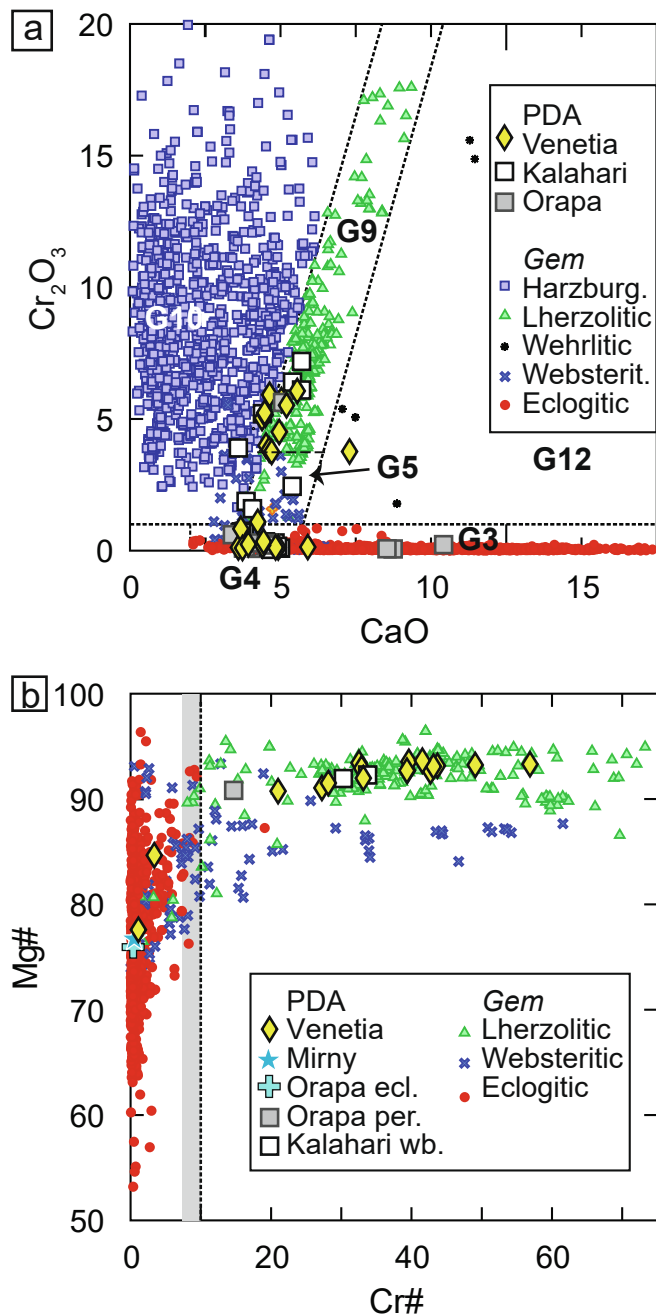


Fig. 6. Major element composition of garnets (a) and clinopyroxenes (b) from Venetia polycrystalline diamond aggregates (PDAs). (a) Cr₂O₃-CaO garnet classification plot (in wt%) with fields after Grütter et al. (2004) for Venetia garnets compared to literature data for PDA garnets from South Africa (Mikhail et al., 2019b; Dobosi and Kurat 2002). Garnet inclusions in gem diamonds worldwide (Stachel et al., 2022a) are shown as small symbols, split into the various paragenesis. G3 = eclogitic, G4, G5 = pyroxenitic/websteritic, G9 = lherzolitic, G10 = harzburgitic, G12 = wehrlitic. (b) Molar Mg# (Mg/[Mg + Fe]*100) versus Cr# (Cr/[Cr + Al]*100) for clinopyroxenes from Venetia PDAs compared to clinopyroxenes in PDAs from Mirny (Sobolev et al., 2016), Orapa (Mikhail et al., 2019b), Museum samples likely from the Kalahari craton origin (Dobosi and Kurat, 2002) and from monocrystalline (*gem*-type) diamonds worldwide. The dashed line is the division between eclogitic and peridotitic (lherzolitic) clinopyroxenes according to Aulbach et al. (2002), the grey band (Cr# 7–10) is the same division according to Stachel & Harris (2008).

4.1. Nitrogen aggregation, mantle residence time and depth of origin

Jacob et al. (2000) deduced a very young formation age (close to kimberlite eruption) for PDAs from this Venetia suite based on trace element heterogeneity in garnets (section 3.5) which could not otherwise be preserved over extended periods of time. While this argument still holds for these PDAs, studies showing plastic deformation and annealing (Rubanova et al., 2012) and highly aggregated nitrogen in Kalahari PDAs (Mikhail et al., 2014b) and in Orapa PDAs (Mikhail et al., 2019b) indicate that not all PDAs worldwide were formed so recently.

Diamond nitrogen aggregation results for Venetia PDAs in this study support the conclusion that not all PDAs are recent, as most of the measured diamond grains in the Venetia suite have high degrees of nitrogen aggregation (Fig. 5, Table 1), which require long mantle residence times of several hundred million years and more typical diamond formation temperatures (Stachel and Harris 2008). However, other PDAs in this suite have low degrees of nitrogen aggregation (Table 1), indicating very short mantle residence times. There is considerable variability within individual PDAs with diamond grains from the same PDA showing significant differences in nitrogen aggregation state (e.g. V1038 Fig. 5, Table 1). Notably, Kalahari PDAs also have a large range of nitrogen aggregation states, including very low degrees (Mikhail et al. 2014b), while Orapa PDAs only have highly aggregated nitrogen (Mikhail et al., 2019b). Thus, assuming typical temperatures for diamond formation in Earth's mantle (900–1300 °C, Stachel and Harris, 2008) these PDA nitrogen aggregation characteristics indicate a range of mantle residence times, indicating that PDAs have formed episodically in Earth's mantle over much of earth history (Jacob et al., 2014).

An alternative explanation to long mantle residence times for the highly aggregated nitrogen in PDAs is that they could have formed deeper in the mantle and resided at higher temperatures. Higher temperatures translate to shorter mantle residence times, based on the thermodynamic parameters of nitrogen diffusion in diamond (Chrenko et al., 1977; Evans and Qi, 1982; Taylor, 1990; Taylor et al., 1996). For example, an average temperature of 1300 °C results in a mantle residence time of only 100 Myr (Table 1). Jacob et al. (2004) provided evidence for temperatures of more than 1370 °C in Venetia PDA suite: Venetia PDA V906 contains websteritic garnet with inclusions of spherical assemblages of iron metal and iron carbide (cohenite) coated by thin layers of FeS, which places the evolution of this PDA at very reducing conditions close to the iron-wüstite buffer. These 'steel spheres' were associated with shrinkage cavities at the interface with their garnet host (see Fig. 2 in Jacob et al., 2004), demonstrating that the assemblage was included as a melt. Experimental phase relations demand temperatures of at least 1370 °C at around 5 GPa for this process (Lord et al., 2009). Jacob et al. (2004) reported similar inclusions in other PDAs (V945, V948, V961) in this Venetia suite. Although these were altered, they show that high formation temperatures (and low fO₂) were not a singular odd occurrence in these PDAs. A significant part of the monocrystalline diamond population from Venetia also formed under unusually reducing conditions (Deines et al., 2001), suggesting a potential link between PDA and *gem*-type diamond formation at this locality.

While there is no indication of generally higher-than-average residence temperatures for PDAs suites from other localities, Jacob et al. (2016) estimated a depth of origin in excess of 10 GPa for one eclogitic Orapa PDA on the basis of microtextural evidence from a syngenetic magnetite corona enveloping a protogenetic Fe-sulphide microinclusion in a diamond crystal. This pressure places the PDA at ca. 320–330 km depth in the mantle, corresponding to depths of at least the geophysical base of the subcratonic lithosphere (Fouch et al., 2004) or the upper part of the asthenosphere under Orapa (Jacob et al. 2016).

In contrast, Jacob and Mikhail (2022) calculated lithospheric pressures of 6.0–7.4 GPa using single garnet geobarometry (Thomson et al., 2021) on the worldwide PDA database, and used these pressures in conjunction with the absence of excess silica in PDA garnets to argue for a broadly lithospheric origin for most PDAs globally. They did however

Table 2a

Average chemical compositions of garnets. Major element oxides are in wt%, trace elements in $\mu\text{g g}^{-1}$. n.m. = not measured. P = peridotitic, w = websteritic, *samples studied by Jacob et al. (2000); +sample studied by Jacob et al. (2004).

	V913	V933	V935	V951	V956	V964	V965	V967	V968	V971	V1045	V1060	V906 ⁺	V911*	V919*	V925*
paragenesis	P	w	w	w	w											
n	8	13	12	7	9	7	6	9	12	10	9	12	5	6	5	5
SiO ₂	42.18	41.48	41.83	41.93	41.81	41.94	41.38	41.77	41.76	42.36	41.22	42.10	41.51	41.98	41.93	41.28
TiO ₂	0.25	0.13	0.12	0.14	0.14	0.16	0.46	0.18	0.30	0.27	0.24	0.24	0.18	0.49	0.40	0.31
Al ₂ O ₃	20.7	19.1	20.4	20.1	19.5	19.4	18.9	19.3	19.3	22.8	20.7	20.9	23.4	22.6	22.3	22.8
Cr ₂ O ₃	3.99	5.92	4.50	5.03	5.23	5.15	6.06	5.72	5.52	1.09	3.83	3.75	0.13	0.14	0.34	0.12
FeO	7.07	6.86	6.94	6.96	6.96	7.20	7.77	7.19	8.14	7.82	6.96	6.92	9.38	8.75	10.8	11.5
MnO	0.37	0.37	0.36	0.38	0.35	0.31	0.39	0.35	0.41	0.37	0.32	0.37	0.31	0.26	0.29	0.30
MgO	21.7	21.1	21.0	21.8	21.3	20.9	19.1	20.8	19.2	21.3	21.6	21.3	18.9	20.9	19.0	18.2
CaO	4.52	4.64	4.96	4.39	4.48	4.50	5.56	5.04	5.20	4.25	4.63	4.71	5.91	4.45	4.44	4.84
Na ₂ O	0.05	0.07	0.05	0.06	0.04	0.05	0.13	0.06	0.11	0.10	0.04	0.05	0.02	0.07	0.07	0.04
K ₂ O	0.01	0.01	0.01	0.01	<0.01	<0.01	0.01	0.01	<0.01	<0.01	<0.01	0.01	0.01	<0.01	0.01	<0.01
Total	100.9	99.6	100.1	100.8	99.8	99.6	99.9	100.4	99.9	100.3	99.6	100.3	99.8	99.6	99.6	99.3
Mg#	87.4	87.1	86.6	88.4	86.5	84.8	81.8	86.2	80.7	85.0	89.5	86.5	80.9	81.0	76.9	75.4
n	8	5	5	6	3	5	6	4	9	4	5	6	4	4	5	5
Li	n.m.	n.m.	n.m.	n.m.												
Th	0.068	0.044	0.039	0.032	0.025	0.035	0.023	0.032	0.079	0.031	0.013	0.028	0.157	<0.01	0.010	<0.01
U	0.063	0.061	0.043	0.036	0.060	0.072	0.023	0.053	0.057	0.030	0.021	0.028	0.072	0.013	0.010	0.020
Nb	0.660	0.820	0.814	0.680	0.655	0.785	0.297	0.982	0.500	0.267	0.379	0.385	0.901	0.205	0.268	0.500
Ta	0.031	0.069	0.073	0.073	0.078	0.055	0.030	0.091	0.045	0.032	0.040	0.036	0.006	0.020	0.030	0.060
La	0.071	0.050	0.066	0.035	0.070	0.074	0.025	0.075	0.140	0.034	0.023	0.037	0.257	0.010	0.012	0.016
Ce	0.538	0.671	0.721	0.412	0.582	0.775	0.247	0.755	0.712	0.184	0.252	0.283	0.861	0.113	0.123	0.169
Pr	0.160	n.m.	0.245	n.m.	n.m.	n.m.	0.133	0.040	0.055	0.064						
Sr	0.391	1.09	0.605	0.471	0.551	0.487	0.498	0.635	0.410	0.196	0.293	0.326	5.66	0.357	0.332	0.407
Nd	1.36	2.57	2.65	1.65	1.68	2.31	1.18	2.47	1.88	0.632	1.18	1.29	0.805	0.468	0.696	0.733
Sm	0.819	1.63	1.24	0.980	1.08	1.10	1.05	1.29	1.07	0.575	0.904	0.857	0.797	0.530	0.602	0.700
Zr	26.3	38.0	18.6	33.5	33.2	24.4	53.1	22.0	26.8	23.3	27.0	19.9	29.7	43.5	41.4	19.0
Hf	0.546	0.474	0.468	0.470	0.544	0.421	0.670	0.394	0.713	0.616	0.598	0.547	0.662	1.07	0.960	0.430
Eu	0.313	0.767	0.415	0.470	0.507	0.432	0.556	0.492	0.415	0.254	0.359	0.344	0.418	0.284	0.331	0.389
Gd	1.24	2.27	1.13	1.57	1.55	1.44	2.11	1.37	1.64	1.28	1.38	1.24	2.51	1.35	1.62	1.95
Tb	0.225	0.325	0.154	0.240	0.221	0.211	0.394	0.179	0.310	0.352	0.278	0.256	0.666	0.375	0.493	0.609
Dy	1.68	2.04	0.913	1.76	1.58	1.68	2.40	1.36	2.33	3.96	2.31	2.25	5.83	3.72	4.82	5.85
Y	9.91	10.6	5.84	10.8	7.29	10.6	11.3	6.86	12.1	31.2	16.4	16.6	38.4	27.8	37.3	43.2
Ho	0.439	n.m.	0.718	n.m.	n.m.	n.m.	1.55	1.08	1.43	1.64						
Er	1.32	1.17	0.689	1.32	0.843	1.41	1.06	0.729	1.88	4.37	2.24	2.27	5.22	3.92	5.19	5.63
Tm	0.233	n.m.	0.351	n.m.	n.m.	n.m.	0.900	0.690	0.880	0.948						
Yb	2.07	1.34	1.00	1.72	1.02	2.04	1.01	1.01	2.13	5.86	3.23	3.15	6.76	5.76	7.07	7.44
Lu	0.396	0.243	0.187	0.310	0.185	0.377	0.149	0.176	0.341	1.01	0.527	0.504	1.09	0.955	1.22	1.20
Sc	112	117	111	134	129	134	101	111	109	134	108	130	78.7	n.m.	n.m.	n.m.
V	260	260	294	288	229	255	142	276	262	347	279	275	n.m.	n.m.	n.m.	n.m.
Co	44.2	42.2	41.9	48.2	42.6	44.2	41.5	45.1	44.5	52.7	41.7	43.2	n.m.	n.m.	n.m.	n.m.
Ni	57.7	53.7	51.2	62.0	57.9	52.6	56.9	60.1	59.0	55.7	53.7	55.7	38.8	n.m.	n.m.	n.m.
Cu	6.63	0.354	0.938	0.358	0.405	0.348	0.285	0.303	0.300	0.383	0.149	0.333	12.7	n.m.	n.m.	n.m.
Zn	17.6	11.8	12.6	15.3	10.7	13.8	14.5	13.1	15.5	21.4	13.4	12.9	31.0	n.m.	n.m.	n.m.

point out that while PDAs as a group do not provide evidence for an asthenospheric origin, individual PDAs from the Venetia and Orapa localities show temperatures and pressures compatible with an origin from below the cratonic lithosphere, and this fact cannot be overlooked in models for their origin.

4.2. Uncoupling of $\delta^{13}\text{C}$ and $\delta^{15}\text{N}$ and indications for diamond fluid compositions

The PDAs neither individually nor collectively show systematic correlations of $\delta^{15}\text{N}$ - with $\delta^{13}\text{C}$ -values (Fig. 10). Instead, large ranges of $\delta^{15}\text{N}$ values (up to 13 ‰) and N concentrations (Fig. S1) observed within individual samples (Figs. 2, 10) are often associated with constant $\delta^{13}\text{C}$ -values (Fig. S6). Uncoupling of N and C isotopes within individual diamonds has been reported before for PDAs from Orapa and the Kalahari suite (Mikhail et al., 2014a) as well as for monocrystalline diamonds from several localities worldwide (Hogberg et al., 2016; Mikhail et al., 2014a), and cannot be explained in terms of a single mixing model for fluids with unique endmembers. Instead, several authors (Hogberg et al., 2016; Petts et al., 2015; Stachel et al., 2022a) suggested isotope fractionation effects between different nitrogen species (e.g. N_2 , NH_3 , NH_4^+) during diamond crystallization in an evolving COH fluid. Nitrogen fractionation factors for the prevalent nitrogen species N_2 , NH_3 , NH_4^+ in

diamond-forming fluids are negative and shift the diamonds to higher $\delta^{15}\text{N}$ values (Petts et al., 2015), while only strongly reducing diamond – fluid pairs containing nitrides have positive fractionation factors causing lower $\delta^{15}\text{N}$ values in diamonds crystallizing from such fluids (Thomassot et al., 2007). Nitrogen fractionation factors are also much larger than isotope fractionation factors for the typical carbon species in COH fluids and diamond (see Stachel et al. 2022b for a comprehensive summary).

Diamond grains in V1064D, one of four analysed fragments of PDA V1064, show an apparent positive trend of $\delta^{15}\text{N}$ values with N – concentrations (Fig. S7), and in the following we explore if this correlation could be caused by a process of Rayleigh fractionation upon diamond precipitation from a single fluid: Adding data from other analysed V1064 fragments (A, B, C) shows that this apparent trend is defined by fragment ‘D’ only, while all other fragments fall either to the high end or the low end of the trend (Fig. S7), thus questioning this apparent correlation. If Rayleigh fractionation was to explain the apparent trend in V1064D, the negative correlation of $\delta^{15}\text{N}$ values with N concentrations would require a positive N isotope fractionation factor which can only be achieved in a highly reducing fluid by fractionation in equilibrium with nitrides (Thomassot et al. 2007). While such fluids are a possibility at Venetia where we have evidence for reducing fluids (Jacob et al. 2004), modelling the correlation by Rayleigh fractionation is impossible as this would require either an unrealistically high N

Table 2b
Average chemical compositions of garnets ctd.

	V934	V940	V942	V945	V948*	V961	V963	V1058	V1061	V1015
paragenesis	w	w	w	w	w	w	w	w	w	w
n	12	8	1	14	5	6	14	4	18	12
SiO ₂	42.24	40.43	40.23	42.38	40.80	40.34	41.69	40.99	42.32	41.40
TiO ₂	0.61	0.27	0.28	0.64	0.23	0.28	0.43	0.30	0.64	0.58
Al ₂ O ₃	22.74	22.42	22.41	21.85	22.96	22.38	23.07	22.70	21.95	20.10
Cr ₂ O ₃	0.20	0.11	0.12	0.82	0.12	0.10	0.24	0.20	0.45	3.76
FeO	8.25	18.07	18.03	7.53	13.06	18.32	9.39	12.63	8.08	9.18
MnO	0.33	0.42	0.42	0.30	0.31	0.42	0.36	0.41	0.33	0.47
MgO	21.81	14.97	15.06	22.29	17.38	14.91	20.38	17.75	21.93	17.62
CaO	3.86	3.63	3.60	3.68	4.93	3.74	3.93	4.41	3.78	7.29
Na ₂ O	0.11	0.10	0.11	0.11	0.05	0.09	0.07	0.07	0.12	0.14
K ₂ O	0.01	0.01	0.01	0.01	<0.01	0.01	0.01	0.01	0.01	0.01
Total	100.2	100.3	100.3	99.6	99.8	100.6	99.6	99.4	99.6	100.6
Mg#	86.0	62.0	62.7	87.0	73.5	62.1	81.6	73.7	86.1	79.6
n	18	18	3	8	6	12	6	7	8	9
Li	0.420	1.24	1.24	0.420	n.m.	1.37	0.320	0.190	0.370	n.m.
Th	0.013	0.044	0.059	0.033	0.010	0.039	<0.01	0.010	0.017	0.033
U	0.013	0.019	0.026	0.017	0.020	0.016	0.011	0.021	0.010	0.020
Nb	0.170	0.090	0.039	0.140	0.540	0.070	0.300	0.470	0.160	0.392
Ta	0.020	0.030	0.064	0.020	0.040	<0.01	0.020	0.040	0.020	0.017
La	0.026	0.097	0.081	0.030	0.031	0.082	0.013	0.028	0.020	0.034
Ce	0.137	0.138	0.110	0.100	0.207	0.188	0.092	0.156	0.097	0.274
Pr	n.m.	n.m.	n.m.	n.m.	0.074	n.m.	n.m.	n.m.	n.m.	0.106
Sr	0.320	0.720	0.861	0.300	0.427	0.620	0.240	0.360	0.220	0.623
Nd	0.371	0.394	0.266	0.358	0.927	0.386	0.444	0.645	0.415	1.19
Sm	0.393	0.415	0.389	0.332	0.857	0.412	0.451	0.616	0.409	1.17
Zr	38.9	11.7	11.8	38.9	44.1	10.8	56.7	35.3	40.3	56.7
Hf	0.970	0.230	0.233	1.04	0.940	0.200	1.21	0.750	0.970	1.36
Eu	0.189	0.223	0.217	0.183	0.477	0.217	0.225	0.317	0.194	0.641
Gd	0.871	1.20	1.24	0.830	2.05	1.16	1.12	1.70	0.832	2.46
Tb	0.218	0.347	0.327	0.170	0.544	0.340	0.324	0.495	0.202	0.534
Dy	2.20	3.57	3.24	1.55	5.35	3.55	3.49	5.19	1.94	3.98
Y	18.3	26.5	27.1	10.4	37.7	26.7	28.7	38.9	15.0	21.0
Ho	n.m.	n.m.	n.m.	n.m.	1.422	n.m.	n.m.	n.m.	n.m.	0.994
Er	2.86	3.70	3.79	1.45	4.56	3.77	4.32	4.96	2.24	2.83
Tm	n.m.	n.m.	n.m.	n.m.	0.743	n.m.	n.m.	n.m.	n.m.	0.449
Yb	4.60	4.78	4.71	2.07	5.82	4.74	6.25	5.84	3.44	3.20
Lu	0.772	0.746	0.736	0.360	0.940	0.754	1.048	0.908	0.571	0.495
Sc	89.0	55.9	55.4	83.4	n.m.	55.1	90.7	78.3	72.2	103
V	305	114	116	205	n.m.	122	289	329	304	255
Co	50.5	47.3	44.8	49.1	n.m.	47.5	53.9	60.2	48.5	40.8
Ni	83.6	14.8	13.6	99.1	n.m.	12.0	83.7	72.6	75.1	24.5
Cu	1.16	0.942	1.39	0.894	n.m.	0.350	0.741	0.422	0.679	0.291
Zn	20.1	85.8	72.0	16.4	n.m.	97.8	27.8	52.5	19.9	15.19

partition coefficient of ca. 20 (compared to the accepted value of 4.4; [Petts et al. 2015](#)) or diamond formation in the mantle at temperatures of around only 400 °C, which is clearly unrealistic ([Fig. S7](#)). Based on this we conclude that the combined evidence from CL, N and C systematics discount PDA formation at Venetia via Rayleigh fractionation of a single fluid, but instead point to separate local diamond growth events with distinct N and C compositions and mixed nitrogen species.

4.3. Sources of diamond-forming fluids from carbon and nitrogen isotopes

Nitrogen and carbon diffusion in diamond is limited to length scales of nanometres (see [Stachel et al., 2022b](#) and references therein), meaning that the heterogeneity of $\delta^{15}\text{N}$ and $\delta^{13}\text{C}$ in the diamond grains as well as small-scale zonation in CL intensity reflect diamond growth processes. Differing CL greyscales in the diamond grains show multiple phases of growth and resorption ([Figs. 3, 4](#)) and taken together with heterogeneity in N concentrations, the broad correlation of $\delta^{15}\text{N}$ - and (in some PDAs) also $\delta^{13}\text{C}$ -values with the CL features ([Fig. 3](#)) indicate episodic diamond growth from compositionally distinct fluids/melts. Aggregates of small (ca. 80 μm) crystallites with dark CL greyscale are often found at the cores of PDAs (e.g. [Fig. 3a](#) – V940A, V941C, V942B, V945A, V1045A) and are the earliest diamond growth event we can identify in the Venetia PDAs. They have $\delta^{13}\text{C}$ values between -21.0 and -24.6 ‰ and low nitrogen concentrations with < 300 at. ppm and

mostly ≈ 40 at. ppm. The $\delta^{15}\text{N}$ values of these cores are $+4.1 \pm 1.5$ ‰ (V1064) and $+5.4 \pm 2.4$ ‰ (V1045; average $+4.7 \pm 2.0$ ‰, green asterisk in [Fig. 10](#)) and plot with most of the Venetia PDAs in the field for organics in subducted oceanic crust and lithosphere ([Fig. 10](#); [Halama et al., 2010](#); [Halama et al., 2014](#)). A few individual diamond SIMS analyses (V940, V961, [Table S1](#)) fall in the field for unmodified lherzolitic mantle ([Cartigny et al., 2014](#)) in [Fig. 10](#), and thus carry no clear subduction signature. Hence, the N and C isotope characteristics clearly indicate a subduction origin for most of the carbon and most of the nitrogen in these PDAs.

4.4. Radiogenic isotopes and $\delta^{18}\text{O}$ values of silicates in PDAs

Analyses of four websteritic garnets ([Jacob et al. 2000](#)) yielded unradiogenic $^{87}\text{Sr}/^{86}\text{Sr}$ isotopic ratios (0.703189 to 0.703589) and unradiogenic initial ϵNdi values of -15.9 to -21.7 ([Table 5](#); [Fig. 9](#)), which is characteristic for LREE enriched material that was left to develop to unradiogenic isotopic composition for long geological time-spans in the lithosphere. $\delta^{18}\text{O}$ values of $+6.69$ to $+8.09$ ‰ in these garnets ([Table 5](#), [Jacob et al. 2000](#)) are higher than $\delta^{18}\text{O}$ values for unchanged mantle (5.4 ± 0.4 ‰; [Mattey et al., 1994](#)) and are a clear indication for subducted seawater altered oceanic crust ([Jacob et al., 1994](#)), consistent with the radiogenic isotope signatures. A similar conclusion can be reached for the two peridotitic garnets and the

Table 3

Average chemical compositions of clinopyroxenes. Major element oxides are in wt%, trace elements in μgg^{-1} . n.m. = not measured. P = peridotitic, w = websteritic.

	V922	V933	V950	V951	V956	V962	V965	V967	V968	V993	V1015	V1026	V1045	V1054	V1060	V947	V961
paragenesis	p	p	p	p	p	p	p	p	p	p	p	p	p	p	p	w	w
n	4	6	4	5	9	8	9	7	7	5	4	4	5	5	8	5	6
SiO ₂	54.45	55.06	54.01	55.01	55.22	55.00	55.37	54.86	55.31	54.38	54.20	54.38	54.95	54.88	54.85	53.42	54.55
TiO ₂	0.46	0.10	0.20	0.11	0.06	0.13	0.47	0.10	0.40	0.10	0.38	0.08	0.14	0.19	0.17	0.15	0.40
Al ₂ O ₃	4.18	2.55	2.59	2.73	2.50	1.95	5.33	2.65	7.02	2.45	2.57	2.32	2.25	2.12	2.26	3.38	5.67
Cr ₂ O ₃	1.66	2.84	5.10	3.93	2.43	1.91	2.97	2.57	4.10	2.84	1.90	2.62	1.62	2.25	1.66	0.18	0.09
FeO	2.66	2.28	1.86	2.03	2.28	2.11	2.26	2.30	1.94	2.15	2.49	2.18	2.18	2.05	2.34	5.50	6.70
MnO	0.10	0.08	0.09	0.10	0.08	0.09	0.06	0.10	0.06	0.09	0.10	0.09	0.09	0.10	0.10	0.09	0.09
MgO	14.61	16.07	14.55	15.68	16.21	17.07	12.88	16.39	11.65	16.40	16.02	16.41	17.35	16.88	17.22	17.01	12.97
CaO	17.33	17.39	16.81	17.18	17.89	19.97	14.99	17.91	13.91	17.64	20.49	18.07	19.17	19.46	19.13	16.19	14.40
Na ₂ O	3.20	2.79	3.45	3.22	2.42	1.88	4.68	2.57	5.72	2.57	1.95	2.40	1.99	2.07	2.02	2.10	3.73
K ₂ O	0.05	0.03	0.05	0.06	0.05	0.04	0.05	0.04	0.05	0.04	0.03	0.04	0.05	0.04	0.04	0.04	0.09
Total	98.7	99.2	98.70	100.1	99.1	100.1	99.1	99.5	100.1	98.64	100.1	98.58	99.8	100.0	99.8	98.05	98.7
n	6	4	4	4	3	6	6	5	7	6	6	3	5	5	6		
Li	n.m.	0.787	n.m.	0.866	0.871	0.829	2.38	1.011	2.10	n.m.	n.m.	n.m.	0.610	n.m.	0.860	n.m.	8.30
Th	0.042	0.112	n.m.	0.074	0.140	0.057	0.087	0.167	0.069	n.m.	0.028	n.m.	0.057	n.m.	0.051	n.m.	0.016
U	0.055	0.053	n.m.	0.059	0.044	0.043	0.043	0.035	0.075	n.m.	<0.01	n.m.	0.021	n.m.	0.027	n.m.	0.017
Nb	1.02	1.67	n.m.	1.11	1.02	1.13	1.070	1.49	0.590	n.m.	0.414	n.m.	0.718	n.m.	1.08	n.m.	0.079
Ta	0.038	0.211	n.m.	0.111	0.109	0.049	0.148	0.153	0.126	n.m.	0.070	n.m.	0.075	n.m.	0.080	n.m.	0.022
La	1.68	7.64	n.m.	3.15	5.16	2.37	3.04	6.30	1.54	n.m.	1.40	n.m.	3.42	n.m.	3.87	n.m.	1.20
Ce	6.90	26.5	n.m.	12.4	17.3	9.24	12.5	25.0	5.75	n.m.	5.21	n.m.	13.2	n.m.	14.1	n.m.	4.43
Pr	1.18	n.m.	1.03	n.m.	n.m.	n.m.	n.m.	n.m.	n.m.								
Sr	155	412	n.m.	204	231	189	215	392	138	n.m.	137	n.m.	221	n.m.	221	n.m.	165
Nd	6.09	21.4	n.m.	11.0	11.9	7.78	11.4	22.9	5.72	n.m.	4.97	n.m.	11.4	n.m.	11.5	n.m.	4.032
Sm	2.14	4.69	n.m.	2.52	2.28	1.64	2.83	5.14	1.73	n.m.	1.62	n.m.	2.47	n.m.	2.38	n.m.	0.90
Zr	29.7	75.6	n.m.	39.2	18.7	14.0	87.1	57.4	104	n.m.	35.3	n.m.	15.3	n.m.	16.6	n.m.	17.7
Hf	2.04	1.71	n.m.	1.95	0.945	0.813	4.19	2.00	3.89	n.m.	2.20	n.m.	1.01	n.m.	0.902	n.m.	1.02
Eu	0.627	1.21	n.m.	0.695	0.646	0.444	0.847	1.30	0.567	n.m.	0.468	n.m.	0.674	n.m.	0.657	n.m.	0.335
Gd	1.38	3.07	n.m.	1.82	1.26	1.07	2.09	3.05	1.38	n.m.	1.14	n.m.	1.56	n.m.	1.37	n.m.	1.04
Tb	0.175	0.297	n.m.	0.162	0.099	0.099	0.242	0.264	0.179	n.m.	0.137	n.m.	0.153	n.m.	0.140	n.m.	0.157
Dy	0.723	1.30	n.m.	0.725	0.455	0.434	1.08	0.912	0.770	n.m.	0.604	n.m.	0.658	n.m.	0.629	n.m.	0.968
Y	1.83	3.64	n.m.	2.04	1.31	1.30	3.55	2.24	3.19	n.m.	2.43	n.m.	2.27	n.m.	2.16	n.m.	3.91
Ho	0.111	n.m.	0.100	n.m.	n.m.	n.m.	n.m.	n.m.	n.m.								
Er	0.207	0.284	n.m.	0.143	0.102	0.118	0.306	0.146	0.342	n.m.	0.227	n.m.	0.219	n.m.	0.183	n.m.	0.389
Tm	0.027	n.m.	0.020	n.m.	n.m.	n.m.	n.m.	n.m.	n.m.								
Yb	0.158	0.161	n.m.	0.080	0.069	0.074	0.167	0.091	0.344	n.m.	0.162	n.m.	0.125	n.m.	0.133	n.m.	0.313
Lu	0.028	0.019	n.m.	0.009	0.017	0.012	0.025	0.019	0.051	n.m.	0.030	n.m.	0.011	n.m.	0.017	n.m.	0.025
Sc	26.2	25.6	n.m.	45.7	21.4	24.4	36.0	27.5	26.9	n.m.	31.2	n.m.	24.7	n.m.	25.0	n.m.	21.9
V	297	416	n.m.	428	375	385	402	442	452	n.m.	497	n.m.	379	n.m.	374	n.m.	379
Co	16.4	20.1	n.m.	19.4	21.9	24.4	24.8	24.4	17.0	n.m.	16.5	n.m.	21.1	n.m.	21.2	n.m.	26.6
Ni	253	399	n.m.	364	468	408	483	525	304	n.m.	202	n.m.	396	n.m.	395	n.m.	97
Cu	n.m.	1.83	n.m.	2.17	5.76	3.08	2.44	2.81	3.25	n.m.	16.73	n.m.	4.96	n.m.	1.97	n.m.	2.76
Zn	n.m.	9.65	n.m.	11.0	11.6	12.9	14.8	12.2	13.4	n.m.	33.0	n.m.	9.6	n.m.	11.0	n.m.	89.0

Table 4

Composition of micas. Major element oxides are in wt%, trace elements in μgg^{-1} . n.m. = not measured. P = peridotitic, w = websteritic.

	V933	V1054	V1060	V940
paragenesis	p	p	p	w
n	12	5	15	7
SiO ₂	38.91	41.92	41.73	39.11
TiO ₂	3.29	1.40	0.85	3.03
Al ₂ O ₃	14.7	12.2	12.2	14.1
Cr ₂ O ₃	1.48	0.433	0.51	0.13
FeO	4.08	3.11	2.92	8.16
MnO	0.04	0.036	0.03	0.03
MgO	21.9	25.3	25.7	19.4
CaO	0.02	0.002	0.01	0.01
Na ₂ O	0.55	0.182	0.11	0.23
K ₂ O	9.72	10.6	10.50	9.69
H ₂ O ⁺	n.m.	n.m.	n.m.	n.m.
Cl ⁻	n.m.	n.m.	n.m.	0.15
F ⁻	n.m.	n.m.	n.m.	0.13
Total	94.63	95.24	94.48	93.92
Mg#	90.5	93.5	94.0	80.9
n	2	3	6	4
Li	14.5	2.00	1.86	8.05
B	1.18	0.98	1.24	n.m.
Ca	90.9	124	185	128
Sc	6.36	3.14	3.99	6.60
Ti	20,870	8284	4748	16,566
V	366	63	109	240
Cr	9038	2519	3178	821
Ni	916	1997	1661	256
Rb	408	589	559	334
Sr	34.5	8.57	6.20	26.8
Y	0.068	0.047	0.035	0.035
Zr	6.80	5.44	1.47	6.66
Nb	36.5	37.2	24.3	30.7
Cs	3.16	4.74	10.6	4.13
Ba	1472	400	436	2209
La	0.061	0.033	0.054	0.062
Ce	0.052	0.036	0.090	0.079
Nd	0.285	0.176	0.092	0.068
Sm	0.320	0.231	0.108	<0.05
Eu	0.094	0.063	0.038	0.048
Gd	0.345	0.191	0.104	<0.08
Hf	0.228	0.169	0.057	0.196
Ta	3.71	3.59	2.29	1.78
Th	0.053	0.035	0.039	0.018
U	0.046	0.030	0.015	0.010

peridotitic cpx measured in this study (Table 5) which also show very unradiogenic ϵNdi values of -25.4 and -29.7 for the garnets and -8.3 for the cpx (Table 5, Fig. 9) indicating an origin from ancient subducted oceanic lithosphere. The apparent Sm-Nd ‘age’ for the cpx-garnet pair in V968 is 106 Ma, thus younger than the Venetia Kimberlite (520.6 ± 4.6 Ma) which is an indication of isotopic disequilibrium. In a Sm-Nd isochron diagram the garnets plot in a linear array subparallel but to less radiogenic $^{143}\text{Nd}/^{144}\text{Nd}$ ratios than the 1.1 Ga old population of Venetia diamond inclusions (Kornneef et al. 2017) (Fig. S8). The regression line through all PDA garnets (Fig. S8) yields an ‘age’ of 428 Ma, thus younger than the host kimberlite, and consistent with a mixing line which would be explained by formation of the garnets from melt-rock reactions. The similarity of the Nd isotopic values with the 1.1 Ga garnet population at Venetia rather than with the 3.0 Ga population (Kornneef et al. 2017) may suggest that the PDAs are unlikely to be temporally related to the 3 Ga diamond population at Venetia.

4.5. Origin of PDA silicates by dynamic metasomatism in the mantle

In terms of mineral assemblage, the most unusual characteristic of PDAs is that silicates and other non-diamond phases (sulphides, carbides, etc.) are only present as accessory phases while the major component is diamond. Their diamond to silicate ratio is thus much closer to monocrystalline diamonds that contain silicate inclusions than

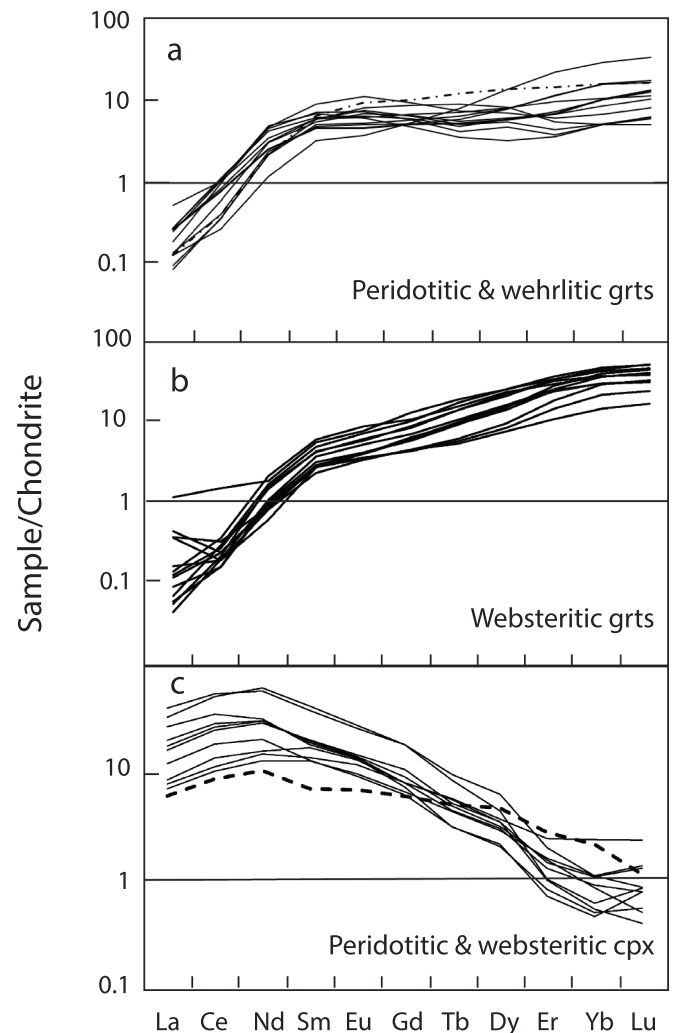


Fig. 7. Chondrite-normalized Rare Earth Element diagrams for peridotitic, wehrlitic (a) and websteritic garnets (b), as well as peridotitic and websteritic (c) clinopyroxenes in polycrystalline diamond aggregates. Dashed line in (a) is wehrlitic garnet V1015. Chondrite values from Sun and McDonough (1989).

most mantle rocks where the situation is reversed, and diamond is the accessory mineral. However, despite a similar diamond to silicate ratio, silicates in PDAs are geochemically distinct from inclusions in monocrystalline diamonds. While databases for these species differ in size by about an order of magnitude, the differences are striking (Jacob and Mikhail, 2022): silicates from PDAs worldwide are predominantly websteritic garnets (57 %) and peridotitic clinopyroxenes (79 %), while in monocrystalline diamond inclusions websteritic garnets are rare (3 %) and clinopyroxenes are most often eclogitic (75 %) (Kiseeva et al., 2013; Stachel and Harris, 2008; Stachel 2014). The other major constituents of the mantle, orthopyroxene and olivine, occur as inclusions in monocrystalline diamonds but are absent in PDAs.

Websterite rocks are olivine-free or olivine-poor pyroxenites (Le Maitre et al., 2002) with compositions broadly intermediate between peridotite and eclogite (Downes, 2007). Generally, and globally, they are the products of melt/rock interactions (Lu et al., 2018 and references therein), and subcratonic lithospheric garnet websterites are typically reaction products of the interaction of melt with mantle rocks (e.g. Rehfeldt et al. 2008; Mallik and Dasgupta 2012; Kiseeva et al. 2016). Given that websterites are typically melt-reaction products it stands to reason that the prevalence of websteritic garnets in PDAs is a result of melt-rock reactions that also produced diamond.

Pintér et al. (2022) explored such melt-rock reactions experimentally

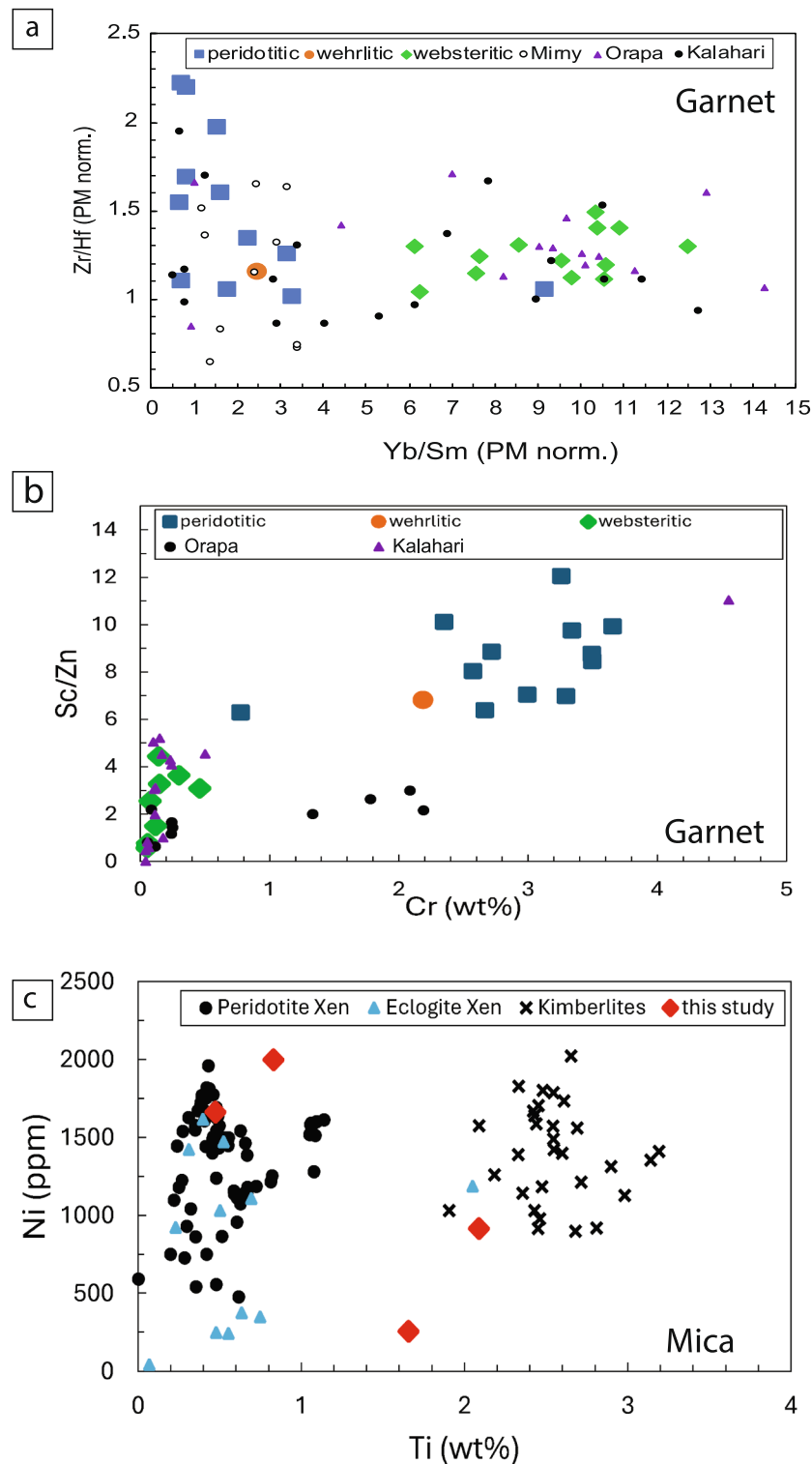


Fig. 8. Zr/Hf ratios vs Yb/Sm ratios normalized to primitive mantle values in (a) Venetia websteritic (green diamonds), peridotitic (blue squares) and wehrlitic (orange dot- V1015) garnets compared to literature data for garnets from PDAs from Mirny, Siberia (open circles represent individual analyses in two PDAs: [Sobolev et al., 2016](#)), Orapa (purple triangles: [Mikhail et al. 2019b](#)) Kalahari craton (black dots: [Dobosi and Kurat, 2002](#)). Yb/Sm is chosen over Lu/Sm to depict the Mirny dataset which does not contain Lu concentrations. (b) Sc/Zn ratios vs Cr concentrations in garnets (symbols as in (a)) (c) Ti vs Ni concentrations in micas from Venetia PDAs (red diamonds) compared to micas found in eclogite xenoliths from Kimberley, South Africa (blue triangles – [Jacob et al., 2009](#)), from kimberlites (crosses – [Giuliani et al., 2016](#); [Delaney et al., 1980](#)) and from mantle xenoliths (black dots – [Erlank et al., 1987](#); [Dawson and Smith, 1975; 1977](#); [Delaney et al., 1980](#); [Giuliani et al., 2013](#); [Giuliani et al., 2014](#); [Giuliani et al., 2016](#); [Grégoire et al., 2002](#); [Jacob et al., 2009](#); [Jones et al., 1982](#); [Matson et al., 1986](#); [Rehfeldt et al., 2008](#); [Rosenbaum 1993](#)). For discussion see text. Primitive Earth's Mantle values from [Sun and McDonough \(1989\)](#). (For interpretation of the references to colour in this figure legend, the reader is referred to the web version of this article.)

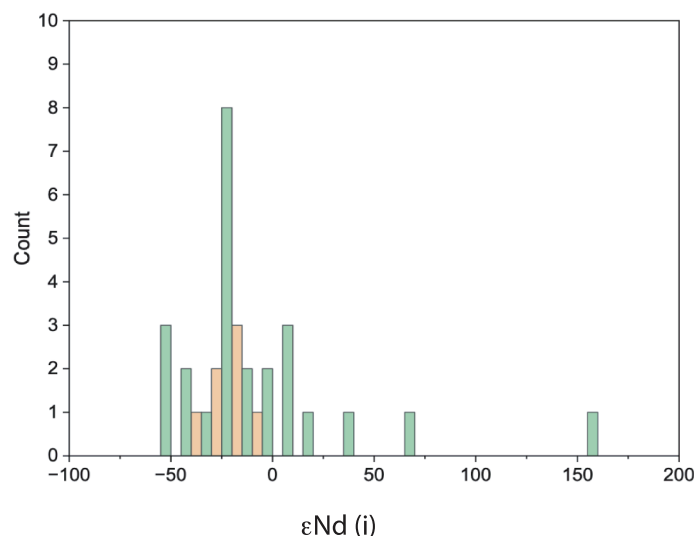


Fig. 9. Histogram of ϵ_{Nd} values for garnets and cpx from Venetia PDAs (orange) compared to ϵ_{Nd} values for peridotitic diamond inclusions from Venetia (Koorneef et al 2017). (For interpretation of the references to colour in this figure legend, the reader is referred to the web version of this article.)

Table 5

Radiogenic isotope compositions and element concentrations determined by isotope dilution, and $\delta^{18}\text{O}$ -values in ‰ relative to SMOW (Standard Mean Ocean Water). Initial ϵ_{Nd} -values ($\epsilon_{\text{Nd}i}$) are calculated for the Venetia kimberlite eruption age of 520.6 ± 4.6 Ma (weighted average of three ages published by Phillips et al., 1999; Griffin et al., 2014).

Sample	mineral	$^{143}\text{Nd}/^{144}\text{Sm}$	2σ	$\epsilon_{\text{Nd}i}$	$^{147}\text{Sm}/^{144}\text{Nd}$	Nd ppm	Sm ppm	$^{87}\text{Sr}/^{86}\text{Sr}$	2σ	$^{87}\text{Rb}/^{86}\text{Sr}$	Rb ppm	Sr ppm	$\delta^{18}\text{O}$
V913	grt	0.512264	1.7E-05	-29.7	0.3376	1.317	0.736	n.m.		n.m.	n.m.	n.m.	n.m.
V968	grt	0.513022	1.4E-05	-25.4	0.4945	1.492	1.221	n.m.		n.m.	n.m.	n.m.	n.m.
V968	cpx	0.512797	8.1E-05	-8.3	0.1719	6.07	1.72	n.m.		n.m.	n.m.	n.m.	n.m.
V911*	grt	0.513271	1.4E-05	-21.7	0.6987	0.4561	0.523	0.703193	9E-05	0.1657	0.016	0.2416	6.49 ± 4
V919*	grt	0.513209	1.7E-05	-18.3	0.6314	0.5165	0.534	0.703589	7E-05	0.1743	0.02	0.296	7.30 ± 2
V925*	grt	0.513178	1.9E-05	-15.9	0.5864	0.856	0.827	0.703189	2E-05	0.0556	0.02	0.963	7.81 ± 3
V948*	grt	0.513219	1.6E-05	-17.7	0.6249	7.16	7.394	0.703379	8E-05	0.1674	0.19	2.988	8.09 ± 5

* From Jacob et al. (2000), n.m. = not measured.

at pressures, temperatures and oxygen fugacities of the deep cratonic lithosphere. They reacted carbonate-bearing melts (carbonated-silicate melt with 30 % SiO_2 and carbonatite with < 10 % SiO_2) with reduced harzburgite and showed that percolation of such melts through the reduced cratonic roots produces zones with distinct mineralogy via melt-rock reactions, whilst also precipitating diamond. Notably, the garnets produced in these experiments (Pintér et al. 2022) have a range of websteritic to wehrlitic compositions which describe a trend towards Mg-rich compositions (Fig. 11). This trend is generally consistent with the trend in compositions seen in the Venetia PDAs, despite differences in grossular content between the garnets produced in these experiments and those in the Venetia PDAs (not shown). This implies that the entire range of garnet compositions seen in the Venetia PDAs could be formed along a single metasomatic reaction pathway.

Reaction path modelling further supports this hypothesis: forward modelling by Mikhail et al. (2021) and Rinaldi et al. (2023) based on the extended Deep Earth Water model by Huang and Sverjensky (2019) showed that dynamic reaction of a single peridotitic fluid with surrounding eclogite (and also the reverse case of a single eclogitic fluid with surrounding peridotite) can create a range of garnet compositions during diamond formation (Fig. 11, grey arrow) that can explain the majority of garnet compositions in PDAs in Venetia as well as globally (Jacob and Mikhail, 2022).

In a model of reaction of migrating and evolving C-O-H fluids/melts with surrounding mantle material (peridotite or subducted oceanic crust in the form of eclogite), silicates would dissolve in and react with the fluid/melt before being re-precipitated together with diamond. Such a model also explains the chemical heterogeneity (section 3.5) and the occurrence of silicates of mixed paragenesis in PDAs, because melt-rock

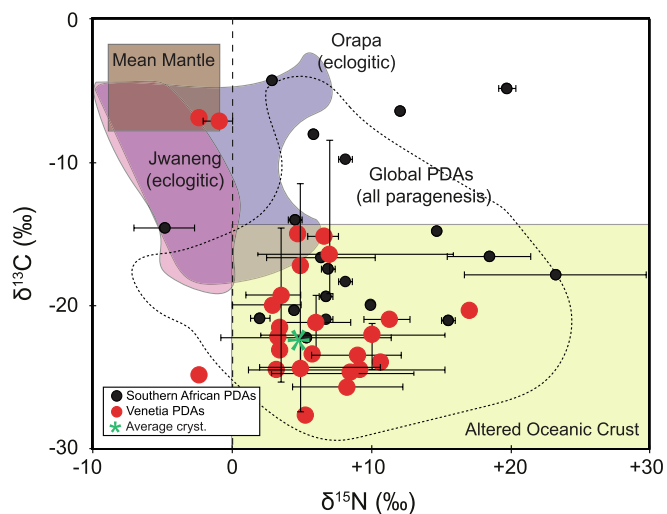


Fig. 10. $\delta^{13}\text{C}$ versus $\delta^{15}\text{N}$ values (data from Table S3) compared to selected types of diamond. Filled circles represent averages while data ranges for individual PDAs are indicated by horizontal and vertical bars. Asterisk is the calculated average for dark-CL crystallite cores of Venetia PDAs. Fields for mean Earth's mantle (Cartigny et al. 2014), Jwaneng and Orapa monocrystalline diamonds with eclogitic and peridotitic inclusions (Cartigny et al. 1998, Cartigny et al., 1999) and for subducted organics (Halama et al. 2010, Halama et al., 2014; Busigny et al., 2019; Cartigny et al. 2014) are shown for comparison.

interactions create small-scale, ephemeral chemical equilibria along the mineral-fluid interface (e.g. Putnis 2009) that would cause precipitation of minerals with differing compositions together with diamond in equilibrium with the evolving fluid/melt composition.

4.6. A model for the origin of PDAs and their role in the deep carbon cycle

Our results show that the Venetia PDA suite is characterised by diamonds that formed from carbon and nitrogen of mainly subduction-related origin and silicates that are metasomatic reaction products derived from ancient subducted oceanic crust and lithosphere. Their multi-scale textural, geochemical and isotopic heterogeneity is a characteristic that is shared with all other PDA suites worldwide and supports models of PDA formation by episodic diamond formation at localised conditions along a metasomatic reaction path in the mantle. Our study supports the statement by Jacob and Mikhail (2022) that “there can be no single model for polycrystalline diamond-formation...”, and here, we take a step further to outline the place of PDAs in a conceptual framework for Earth’s deep carbon cycle.

In their recent review, Foley et al. (2024) emphasized the importance of spatial scale for carbon storage (and release) in Earth’s mantle. Over their geological history, the Thermal Boundary Layer (TBL) and the roots of cratons have accumulated a mixture of rock lithologies, including lithosphere stabilized during craton formation and subduction

of oceanic crust as well as solidification of migrating deep silicate and carbonate melts. Variability in lithologies, chemical potential, pH and fO_2 at relatively small scale, provide reactive ingredients for melt-rock interactions and diamond precipitation explored by Pintér et al. (2022) and Mikhail et al. (2021). Important agents interacting with these lithologies in the TBL and the cratonic roots are asthenospheric melts derived from much higher pressures where conditions are exceptionally reducing and Fe-Ni metals are stable (Rohrbach et al., 2011). The few experimental studies available show that these reduced melts are highly magnesian (ca. 25–30 wt%; Jakobsson and Holloway 2008; Litasov et al., 2014). These melts are generated by mantle upwelling and cross the solidus at depths of around 270 km, with the exact depth depending on the local geotherm and particularly on water activity (Fig. 12a). When they encounter other lithologies that have accumulated over time in the thermal boundary layer and cratonic roots, these migrating melts will react to form new rock types and may also deposit diamond (Fig. 12b), primarily because of the strong and locally variable redox contrast between the reduced melts and more oxidised rocks they meet.

The reaction of extremely magnesian melts (broadly komatiitic in composition) with peridotite has been modelled with a view to explaining the composition of cratonic roots, showing that this process consumes olivine and produces websterites (Tomlinson and Kamber, 2021; Walsh et al., 2023). However, these models investigated higher

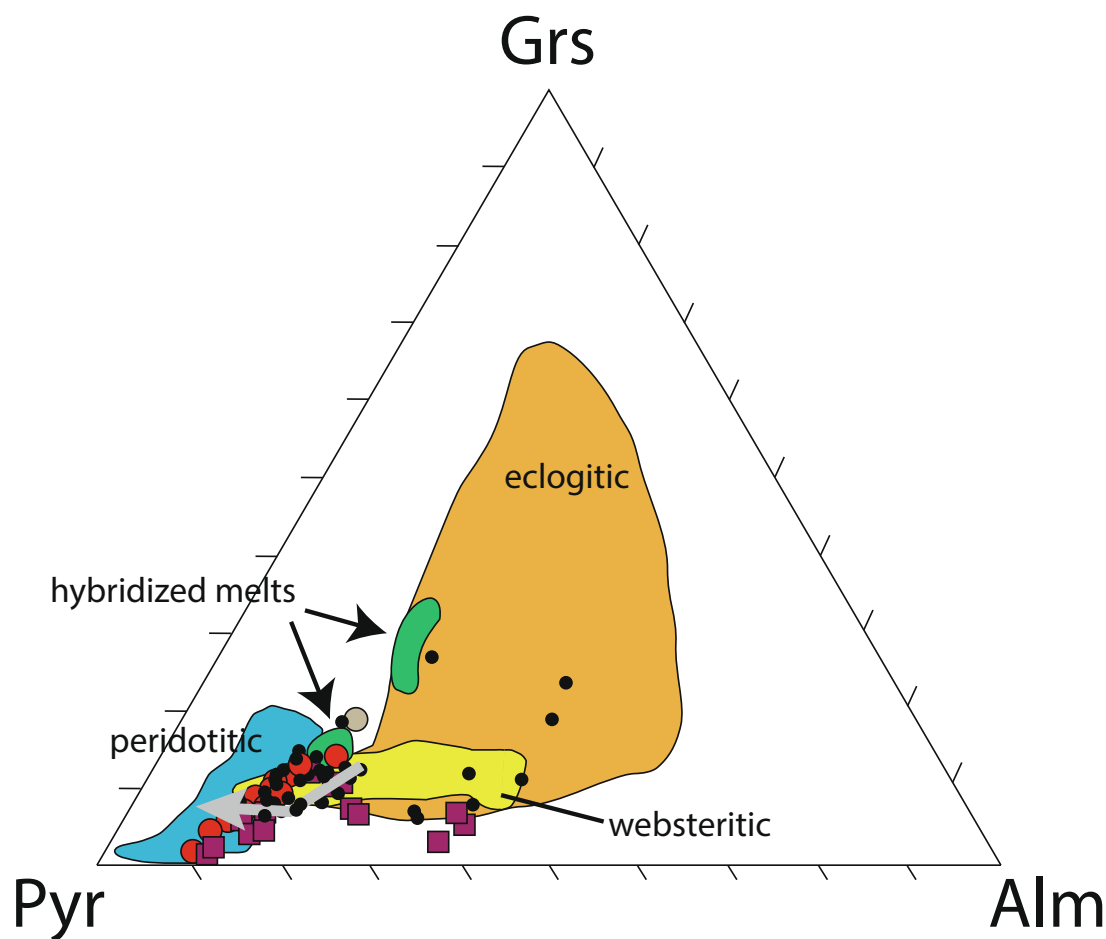


Fig. 11. Fe-Mg-Ca composition of garnets from websteritic (magenta squares), peridotitic (red circles) and wehrlitic (grey circle) PDAs compared to literature data (black dots: Kalahari and Orapa suites; Dobosi and Kurat, 2010; Mikhail et al., 2019b). Thick grey arrow is the trend of predicted garnet compositions in a model of progressive metasomatism and diamond formation at 5GPa and 1000 °C (Mikhail et al., 2021; Rinaldi et al., 2023) starting from a peridotitic garnet composition. Fields for hybridized experimental melt compositions after progressive metasomatism from Pintér et al. (2022) and fields for peridotitic, websteritic and eclogitic garnets included in diamond from Stachel et al. (2022a). (For interpretation of the references to colour in this figure legend, the reader is referred to the web version of this article.)

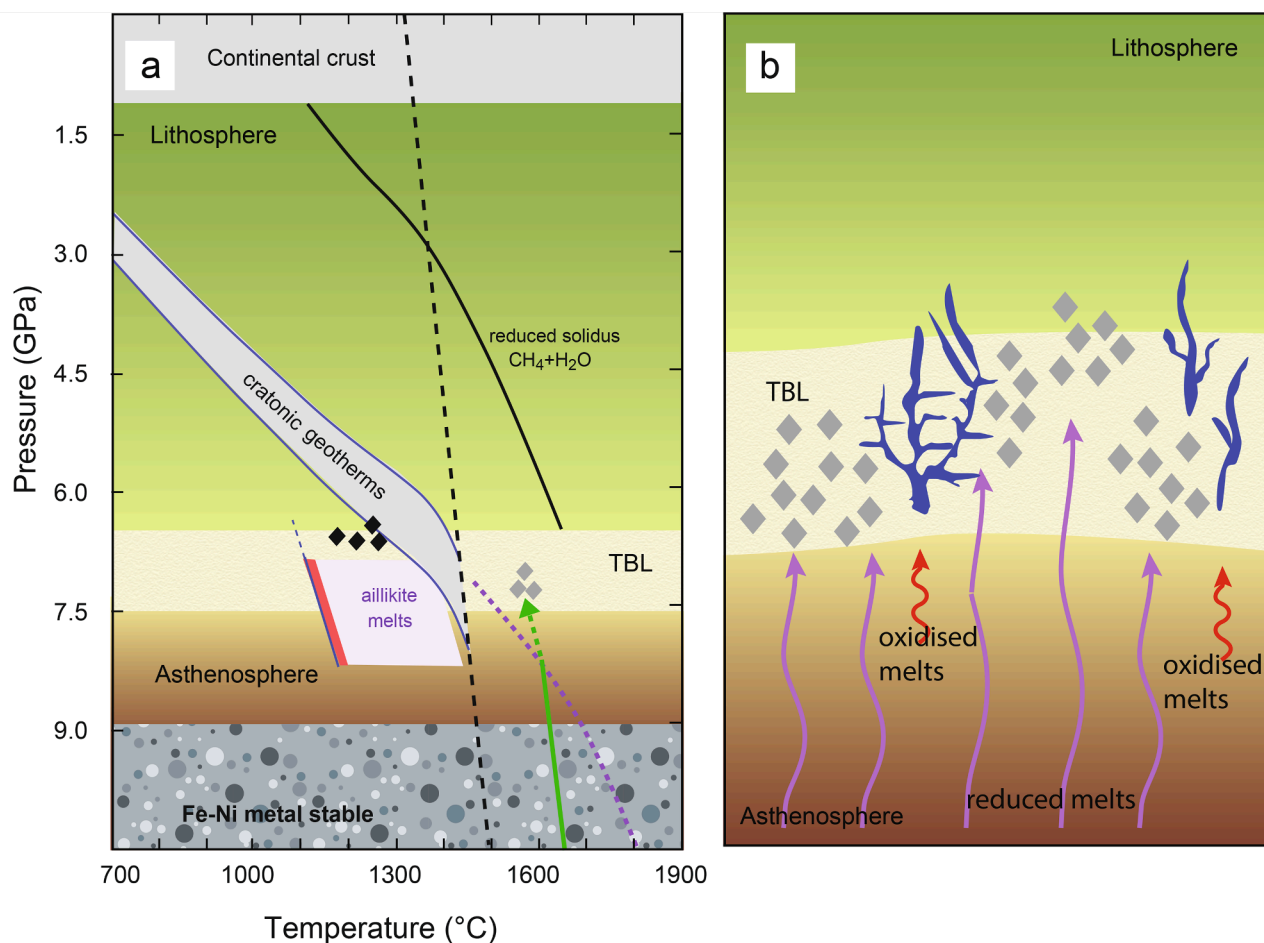


Fig. 12. Conceptual model for the formation of PDAs by small scale reducing asthenospheric melts (modified after [Foley et al. 2024](#)). (a) Realized pressure and temperature regime with melting curves for realistic variations of fO_2 with depth. Relevant melts at these depths are mainly carbonate melts with 10–30% SiO_2 (aillikites) and carbonatites (red area along the solidus). These melts can precipitate diamonds by redox freezing in the cratonic roots. Upwelling of reducing asthenospheric mantle upwelling undergoes melting at the solidus (dotted line), and these melts solidify in the Thermal Boundary Layer (TBL) or cratonic lithosphere by melt-rock reactions while depositing PDAs (grey diamonds). (b) The TBL and roots of the cratons present a potentially reactive area due to the variability on small scales of lithologies and fO_2 that accumulated there over geological timescales, including impregnation of oxidised (red arrows) melts precipitating carbon as carbonates (blue dyke system). Small-scale reducing melts from the asthenosphere (purple arrows) don't attain sufficiently high oxidation state to form carbonate and therefore deposit polycrystalline diamond (grey diamonds) in the TBL and the cratonic roots. (For interpretation of the references to colour in this figure legend, the reader is referred to the web version of this article.)

temperatures (and thus proportions of melt) and did not consider the reduced state of the melts, nor the interaction with rocks other than peridotite. If these reduced melts encounter eclogites that originate from subducted slabs, the higher Al_2O_3 content of eclogite relative to peridotite is likely to promote the formation of websteritic garnets, consistent with the silicates in PDAs. Reaction of the same melts with neighbouring peridotite will remove olivine, and at low temperatures with small amounts of melt will promote the formation of clinopyroxene ([Tomlinson and Kamber, 2021](#)). These melt-rock reactions also deposit diamond ([Pintér et al. 2022](#)) and could be the major process for the formation of PDAs, while explaining the prevalence of websteritic garnets in their silicate suite.

Carbon as well as nitrogen for the diamonds can have various and mixed origins: they may be supplied with the reducing asthenospheric melts, which have low but not insignificant solubility for carbon ([Mysen et al. 2009](#)) and nitrogen ([Roskocz et al., 2013](#)) or from pre-existing carbonate material. In both cases the ultimate source could be oceanic crust and lithosphere now stored in the cratonic lithosphere or subducted as deep as the transition zone, where it stagnated and was remobilized to react with overlying mantle ([Cai et al., 2021](#)).

By this process of melt-rock reaction, PDAs would form episodically at different depths in the deep lithosphere or above the transition zone

(150 – 400 km), while differing local conditions determine the specific mineral paragenesis trapped in the PDAs as well as the chemical and isotopic composition of silicates and diamonds.

[Moore and Helmstaedt \(2023\)](#) proposed a model that links PDAs with the kimberlitic megacryst suite via episodic and dynamic metasomatism in the lithosphere induced by a single thermal event immediately prior to kimberlite eruption. They based their model on textural and geochemical similarities between megacrysts and PDAs, including high temperatures of 1400 °C for some megacryst suites ([Gurney et al., 1979](#)) which are in the range that could account for the high degree of nitrogen aggregation in many PDAs. [Moore and Helmstaedt \(2023\)](#) include CLIPPIR diamonds ([Smith et al., 2016](#)) in their model, based on their similar range in $\delta^{13}C$ values with PDAs which overlaps with $\delta^{13}C$ values for altered oceanic crust ([Li et al., 2019](#)). However, CLIPPIR diamonds are more often interpreted to originate at much deeper, sublithospheric levels ([Smith et al., 2016](#); [Shirey et al. 2024](#)). A distinct characteristic of CLIPPIR diamonds is that they contain very low or undetectable nitrogen (type II diamonds; [Smith et al., 2016](#)) or, where they do contain nitrogen, it is highly aggregated (type IaB; [Banas et al., 2007](#); [Tschauner et al., 2018](#)). Intriguingly, this is similar to the Venetia PDAs, where some of the fine-grained low CL-intensity crystallites in the cores have low contents of highly aggregated nitrogen (e.g. V911),

suggesting a sublithospheric origin of this earliest episode of PDA formation at Venetia.

5. Conclusion

The Venetia polycrystalline diamond aggregates present a dynamic picture of diamond formation in the Earth's mantle at a single locality that corroborates and strengthens evidence from other PDA localities worldwide for their formation by episodic melt/fluid-rock reactions in the mantle. We propose that low-volume melts formed in the asthenosphere in reducing conditions are the main metasomatic agents. These melts could be triggered by the same mantle upwelling or plume events that led to the eruption of the host kimberlite. Alternatively, they may be temporally unrelated deep mantle melting events that used the same pathways through the asthenosphere and lithosphere, episodically producing PDAs and monocrystalline diamonds as suggested by the existence of two temporally distinct diamond populations at Venetia (Koornneef et al., 2017). Given that PDAs in some kimberlites can amount to 20 % of the diamond production, we suggest that PDA formation presents a significant mechanism for (re-)mobilization and storage of carbon as diamond in the cratonic roots and thermal boundary layer that has been operating episodically over extended periods of geological time.

CRedit authorship contribution statement

Dorrit E. Jacob: Writing – review & editing, Writing – original draft, Visualization, Supervision, Resources, Project administration, Methodology, Investigation, Funding acquisition, Formal analysis, Data curation, Conceptualization. **Richard A. Stern:** Writing – review & editing, Methodology, Formal analysis. **Janina Czas:** Methodology, Investigation, Formal analysis. **Magnus Reutter:** Investigation, Formal analysis. **Sandra Piazzolo:** Writing – original draft, Methodology, Formal analysis. **Thomas Stachel:** Writing – review & editing, Writing – original draft, Visualization, Resources, Methodology, Investigation.

Data availability

Data are available through ANU Data Commons at <https://doi.org/10.25911/h76m-fg35>.

Declaration of competing interest

The authors declare that they have no known competing financial interests or personal relationships that could have appeared to influence the work reported in this paper.

Acknowledgments

Samples were made available by the DeBeers Group and research presented here was in parts funded by the Australian Research Council (CE110001017). Some analytical data were obtained using instrumentation funded by DEST Systemic Infrastructure Grants, ARC LIEF, NCRIS/AuScope, industry partners and Macquarie University. John Chapman is gratefully acknowledged for his support with FTIR spectra decomposition. The authors thank Matthew Hardman, Sami Mikhail, Katie Smart and three anonymous reviewers for their constructive comments and AE Dmitri Ionov for handling the manuscript. This is contribution 1758 from the ARC Centre of Excellence for Core to Crust Fluid Systems (<http://www.cafs.mq.edu.au>) and 1552 in the GEMOC Key Centre (<http://www.gemoc.mq.edu.au>).

Appendix A. Supplementary material

Supplementary table S1 contains detail on PDA associated mineral assemblage, table S2 are LA-ICPMS trace element results for reference

materials NIST SRM 610 and USGS BCR2G, table S3 lists SIMS $\delta^{13}\text{C}$, $\delta^{15}\text{N}$ and N concentrations. Figure S1 depicts box and whisker plots for nitrogen concentration data tabulated in Table S3, figure S2 presents CL images for most measured PDAs with SIMS spots indicated, figure S3 shows Scanning Electron Images for PDAs shown in Fig. 2, figure S4, shows a distribution diagram for disorientation angles between diamond grains measured by EBSD, figure S5 presents primitive mantle normalized trace element spidergrams for garnets and cpx, figure S6 shows a plot of $\delta^{15}\text{N}$ values vs nitrogen concentrations for PDAs with uncoupled C-N isotope systematics, figure S7 show $\delta^{15}\text{N}$ and N concentrations in V1064, and figure S8 is a Sm-Nd isochron diagram. Supplementary material to this article can be found online at <https://doi.org/10.1016/j.gca.2024.10.021>.

References

- Armstrong, J.F., 1995. CITZAF: a package of correction programs for the quantitative electron microbeam X-ray analysis of thick polished materials, thin films, and particles. *Microbeam Anal.* 4, 177–200.
- Aulbach, S., Stachel, T., Viljoen, K.S., Brey, G.P., Harris, J.W., 2002. Eclogitic and websteritic diamond sources beneath the Limpopo Belt – is slab-melting the link? *Contrib. Mineral. Petrol.* 143, 143–156.
- Banas, A., Stachel, T., Muehlenbachs, K., McCandless, T.E., 2007. Diamonds from the Buffalo Head Hills, Alberta: Formation in a non-conventional setting. *Lithos* 93, 199–213.
- Boyd, S., Kiflawi, I., Woods, G., 1994. The relationship between infrared absorption and the A defect concentration in diamond. *Philos. Mag. B* 69 (6), 1149–1153.
- Boyd, S., Kiflawi, I., Woods, G., 1995. Infrared absorption by the B nitrogen aggregate in diamond. *Philos. Mag. B* 72 (3), 351–361.
- Busigny, V., Cartigny, P., Laverne, C., Teagle, D., Boniface, M., Agrinier, P., 2019. A reassessment of the nitrogen geochemical behavior in upper oceanic crust from Hole 504B: Implications for subduction budget in Central America. *Earth Planet. Sci. Lett.* 525, 115–135.
- Cai, R., Liu, J.G., Pearson, D.G., Li, D.X., Xu, Y., Liu, S.A., Chu, Z., Chen, L.H., Li, S.G., 2021. Oxidation of the deep big mantle wedge by recycled carbonates: constraints from highly siderophile elements and osmium isotopes. *Geochim. Cosmochim. Acta* 295, 207–223.
- Cartigny, P., Harris, J.W., Phillips, D., Girard, M., Javoy, M., 1998. Subduction-related diamonds? The evidence for a mantle-derived origin from coupled $\delta^{13}\text{C}$ - $\delta^{15}\text{N}$ determinations. *Chem. Geol.* 147, 147–159.
- Cartigny, P., Harris, J.W., Javoy, M., 1999. Eclogitic, peridotitic and metamorphic diamonds and the problems of carbon recycling—the case of Orapa (Botswana). In: 7th International Kimberlite Conference Extended Abstract, pp. 117–124.
- Cartigny, P., Palot, M., Thomassot, E., Harris, J.W., 2014. Diamond formation: a stable isotope perspective. *Annu. Rev. Earth Planet. Sci.* 42, 699–732.
- Chrenko, R.M., Tuft, R.E., Strong, H.M., 1977. Transformation of state of nitrogen in diamond. *Nature* 270, 141–144.
- Czas, J., Stachel, T., Pearson, D.G., Stern, R.A., Read, G.H., 2018. Diamond brecciation and annealing accompanying major metasomatism in eclogite xenoliths from the Sask Craton, Canada. *Mineral. Petrol.* 112, 311–323.
- Davey, R., Garside, J., 2000. From Molecules to Crystallizers - An Introduction to Crystallization. Oxford University Press, New York.
- Dawson, J.B., Smith, J.V., 1975. Chemistry and origin of phlogopite megacrysts in kimberlite. *Nature* 253 (5490), 336–338.
- Dawson, J.B., Smith, J.V., 1977. The MARID (mica-amphibole-rutile-ilmenite-diopside) suite of xenoliths in kimberlite. *Geochim. Cosmochim. Acta* 41(2), 309–310, IN309.
- Deines, P., Harris, J.W., Gurney, J.J., 1993. Depth-related carbon isotope and nitrogen concentration variability in the mantle below the Orapa kimberlite, Botswana, Africa. *Geochimica et Cosmochimica Acta* 57 (12), 2781–2796.
- Deines, P., Viljoen, F., Harris, J.W., 2001. Implications of the carbon isotope and mineral inclusion record for the formation of diamonds in the mantle underlying a mobile belt: Venetia, South Africa. *Geochim. Cosmochim. Acta* 65, 813–838.
- Delaney, J.S., Smith, J.V., Carswell, D.A., Dawson, J.B., 1980. Chemistry of micas from kimberlites and xenoliths—II. Primary- and secondary-textured micas from peridotite xenoliths. *Geochim. Cosmochim. Acta* 44 (6), 857–872.
- Dobosi, G., Kurat, G., 2002. Trace element abundances in garnets and clinopyroxenes from diamondites—a signature of carbonatitic fluid. *Mineral. Petrol.* 76, 21–38.
- Dobosi, G., Kurat, G., 2010. On the origin of silicate-bearing diamondites. *Mineral. Petrol.* 99, 29–42.
- Downes, H., 2007. Origin and significance of spinel and garnet pyroxenites in the shallow lithospheric mantle: Ultramafic massifs in orogenic belts in Western Europe and NW Africa. *Lithos* 99 (1), 1–24.
- Erlank, A.J., Waters, F.G., Hawkesworth, C.J., Haggerty, S.E., Allsopp, H.L., Rickard, R. S., Menzies, M.A., 1987. Evidence for mantle metasomatism in peridotite nodules from the Kimberley pipes, South Africa. *Mantle Metasomatism* 221–311.
- Evans, T., Qi, Z., 1982. The kinetics of the aggregation of nitrogen atoms in diamond. *Proc. r. Soc. A* 381, 159–178.
- Foley, S.F., Chen, C., Jacob, D.E., 2024. The effects of local variations in conditions on carbon storage and release in the continental mantle. *National Science Rev.* nwa098.

- Fouch, M.J., James, D.E., VanDecar, J.C., van der Lee, S., Group, K.S., 2004. Mantle seismic structure beneath the Kaapvaal and Zimbabwe cratons. *S. Afr. J. Geol.* 107, 33–44.
- Fouré, F., Lécuyer, C., Demeny, A., Boulvais, P., Lange, L., Jacob, D.E., Kovacs, I., 2017. 2H/1H measurements of amphiboles and nominally anhydrous minerals (clinopyroxene, garnet and diamond) using high-temperature CF-EA-PP-IRMS. *Rapid Commun. Mass Spectrom.* 31, 2066–2072.
- Gaillou, E., Post, J., Rose, T., Butler, J., 2012. Cathodoluminescence of natural, plastically deformed pink diamonds. *Microsc. Microanal.* 18, 1292–1302.
- Gautheron, C., Cartigny, P., Moreira, M., Harris, J.W., Allegre, C.J., 2005. Evidence for a mantle component shown by rare gases, C and N isotopes in polycrystalline diamonds from Orapa (Botswana). *Earth Planet. Sci. Lett.* 340, 559–572.
- Giuliani, A., Phillips, D., Fiorentini, M.L., Kendrick, M.A., Maas, R., Wing, B.A., Woodhead, J.D., Bui, T.H., Kamenetsky, V.S., 2013. Mantle oddities: A sulphate fluid preserved in a MARID xenolith from the Bultfontein kimberlite (Kimberley, South Africa). *Earth Planet. Sci. Lett.* 376, 74–86.
- Giuliani, A., Phillips, D., Kamenetsky, V.S., Kendrick, M.A., Wyatt, B.A., Goemann, K., Hutchison, G., 2014. Petrogenesis of Mantle Polymict Breccias: Insights into Mantle Processes Coeval with Kimberlite Magmatism. *J. Petrol.* 55 (4), 831–858.
- Giuliani, A., Phillips, D., Kamenetsky, V.S., Goemann, K., 2016. Constraints on kimberlite ascent mechanisms revealed by phlogopite compositions in kimberlites and mantle xenoliths. *Lithos* 240–243, 189–201.
- Goss, J.P., Briddon, P.R., Hill, V., Jones, R., Rayson, M.J., 2014. Identification of the structure of the 3107 cm⁻¹ H-related defect in diamond. *J. Phys. Condens. Matter* 26, 145801.
- Grégoire, M., Bell, D., Le Roex, A., 2002. Trace element geochemistry of phlogopite-rich mafic mantle xenoliths: their classification and their relationship to phlogopite-bearing peridotites and kimberlites revisited. *Contrib. Mineral. Petrol.* 142 (5), 603–625.
- Griffin, W.L., Powell, W.J., Pearson, N.J., O'Reilly, S.Y., 2008. GLITTER: data reduction software for laser ablation ICP-MS. In: Sylvester, P. (Ed.), *Laser Ablation-ICP-Mass Spectrometry in the Earth Sciences: Current Practices and Outstanding Issues*. Mineralogical Society of Canada Short Course Series, Toronto, pp. 308–311.
- Griffin, W.L., Batumike, J.M., Greau, Y., Pearson, N.J., Shee, S.R., O'Reilly, S.Y., 2014. Emplacement ages and sources of kimberlites and related rocks in southern Africa: U-Pb ages and Sr-Nd isotopes of groundmass perovskite. *Contrib. Mineral. Petrol.* 168, 10–32.
- Grütter, H.S., Gurney, J.J., Menzies, A.H., Winter, F., 2004. An updated classification scheme for mantle-derived garnet, for use by diamond explorers. *Lithos* 77, 841–857.
- Gurney, J.J., Boyd, F.R., 1982. Mineral intergrowths with polycrystalline diamonds from the Orapa Mine. Botswana. *Carnegie Inst. Yearbook* 267–273.
- Gurney, J., Jakob, W., Dawson, J., 1979. Megacrysts from the Monastery kimberlite pipe, South Africa. *The Mantle Sample: Inclusion in Kimberlites and Other Volcanics* 16, 227–243.
- Halama, R., Bebout, G.E., John, T., Schenk, V., 2010. Nitrogen recycling in subducted oceanic lithosphere: The record in high- and ultrahigh-pressure metabasaltic rocks. *Geochim. Cosmochim. Acta* 74 (5), 1636–1652.
- Halama, R., Bebout, G.E., John, T., Scambelluri, M., 2014. Nitrogen recycling in subducted mantle rocks and implications for the global nitrogen cycle. *Int. J. Earth Sci.* 103, 2081–2099.
- Heaney, P.J., Vicenzi, E.P., De, S., 2005. Strange diamonds: the mysterious origins of carbonado and framesite. *Elements* 1 (2), 85–89.
- Hin, R.C., Morel, M., Nebel, O., Mason, P.R., van Westrenen, W., Davies, G.R., 2009. Formation and temporal evolution of the Kalahari sub-cratonic lithospheric mantle: Constraints from Venetia xenoliths, South Africa. *Lithos* 112, 1069–1082.
- Hogberg, K., Stachel, T., Stern, R.A., 2016. Carbon and nitrogen isotope systematics in diamond: Different sensitivities to isotopic fractionation or a decoupled origin? *Lithos* 265, 16–30.
- Huang, F., Sverjensky, D.A., 2019. Extended Deep Earth Water Model for predicting major element mantle metasomatism. *Geochim. Cosmochim. Acta* 254, 192–230.
- Jacob, D.E., 2006. High sensitivity analysis of trace element poor geological reference glasses by laser-ablation inductively coupled plasma mass spectrometry (LA-ICP-MS). *Geostandards Geoanalytical Res.* 30, 221–235.
- Jacob, D.E., Mikhail, S., 2022. Polycrystalline Diamonds from Kimberlites: Snapshots of Rapid and Episodic Diamond Formation in the Lithospheric Mantle, in: Shirey, S.B., Pearson, D.G., Nestola, F., Smit, K.V., Stachel, T., Moses, T. (Eds.), *Diamond. Min. Soc. America, Chantilly, Virginia*, 167–189.
- Jacob, D.E., Jagoutz, E., Lowry, D., Matthey, D., Kudrjavtseva, G., 1994. Diamondiferous eclogites from Siberia: Remnants of Archean oceanic crust. *Geochim. Cosmochim. Acta* 58, 5191–5207.
- Jacob, D.E., Viljoen, K.S., Grassineau, N., Jagoutz, E., 2000. Remobilization in the cratonic lithosphere recorded in polycrystalline diamond. *Science* 289, 1182–1185.
- Jacob, D.E., Kronz, A., Viljoen, K.S., 2004. Cohenite and native iron inclusions in garnets from polycrystalline diamonds. *Contrib. Mineral. Petrol.* 146, 566–576.
- Jacob, D.E., Viljoen, F., Grassineau, N., 2009. Eclogite xenoliths from Kimberley, South Africa – a case study of mantle metasomatism in eclogites. *Lithos* 112, 1002–1013.
- Jacob, D.E., Wirth, R., Enzmann, F., Kronz, A., Schreiber, A., 2011. Nano-inclusion suite and High Resolution Micro-Computed-Tomography of polycrystalline diamond (framesite) from Orapa. Botswana. *Earth Planet. Sci. Lett.* 308, 307–316.
- Jacob, D.E., Dobrzhinetskaya, L., Wirth, R., 2014. New insight into polycrystalline diamond genesis from modern nanoanalytical techniques. *Earth Sci. Rev.* 136, 21–35.
- Jacob, D.E., Piazzolo, S., Schreiber, A., Trimby, P., 2016. Redox-freezing and nucleation of diamond via magnetite formation in the Earth's mantle. *Nat. Comm.* 7, 11891.
- Jakobsson, S., Holloway, J.R., 2008. Mantle melting in equilibrium with an Iron-Wüstite-Graphite buffered COH-fluid. *Contrib. Mineral. Petrol.* 155 (2), 247–256.
- Jochum, K.P., Nehring, F., 2006. GeoReM Preferred Values, *georem.mpch-mainz.gwdg.de*.
- Jones, A.P., Smith, J.V., Dawson, J.B., 1982. Mantle Metasomatism in 14 Veined Peridotites from Bultfontein Mine. South Africa. *The Journal of Geology* 90 (4), 435–453.
- Kaminsky, F.V., Galimov, E.M., Genshaft, Y.S., Ivanovskaya, I.N., Klyuev, Y.A., Rovsha, V.S., Sandomirskaya, S.M., Smirnov, V.I., 1981. Boart with a garnet from the Mir pipe (Yakutia). *Dokl. Akad. Nauk SSSR* 256 (256), 674–677.
- Kirkley, M.B., Gurney, J.J., Rickard, R.S., 1995. Jwaneng Framesites: Carbon isotopes and intergrowth compositions, in: Meyer, H.O.A., Leonardos, O.H. (Eds.), *Diamonds: characterization, genesis and exploration*. CPRM Spec Publ pp. 127–135.
- Kiseeva, E.S., Yaxley, G.M., Stepanov, A.S., Tkalcic, H., Litasov, K.D., Kamenetsky, V.S., 2013. Metapyroxenite in the mantle transition zone revealed from majorite inclusions in diamonds. *Geology* 41 (8), 883–886.
- Kiseeva, E.S., Wood, B.J., Ghosh, S., Stachel, T., 2016. The pyroxenite - diamond connection. *Geochem. Persp. Lett.* 2, 1–9.
- Kjarsgaard, B.A., de Wit, M., Heaman, L.M., Pearson, D.G., Stiefenhofer, J., Janusczyk, N., Shirey, S.B., 2022. A Review of the Geology of Global Diamond Mines and Deposits. *Rev. Mineral. Geochem.* 88 (1), 1–117.
- Koornneef, J.M., Gress, M.U., Chinn, I.L., Jelsma, H.A., Harris, J.W., Davies, G.R., 2017. Archean and Proterozoic diamond growth from contrasting styles of large-scale magmatism. *Nat. Comm.* 8, 648.
- Kurat, G., Dobosi, G., 2000. Garnet and diopside-bearing diamondites (framesites). *Mineral. Petrol.* 69, 142–159.
- Le Maitre, R.W., Streckeisen, A., Zanettin, B., Le Bas, M.J., Bonin, B., Bateman, P. (Eds.), 2002. *Igneous Rocks: A Classification and Glossary of Terms: Recommendations of the International Union of Geological Sciences Subcommittee on the Systematics of Igneous Rocks*, 2nd ed. Cambridge University Press, Cambridge.
- Li, K., Pearson, D.G., Stachel, T., 2019. Diamond isotope compositions indicate altered igneous oceanic crust dominates deep carbon cycling. *Earth Planet. Sci. Lett.* 516, 190–201.
- Litasov, K.D., Shatskiy, A., Ohtani, E., 2014. Melting and subsolidus phase relations in peridotite and eclogite systems with reduced COH fluid at 3–16 GPa. *Earth Planet. Sci. Lett.* 391, 87–99.
- Lord, O.T., Walter, M.J., Dasgupta, R., Walker, D., Clark, S.M., 2009. Melting in the Fe-C system to 70 GPa. *Earth Planet. Sci. Lett.* 284 (1), 157–167.
- Lu, J., Griffin, W.L., Tilhac, R., Xiong, Q., Zheng, J., O'Reilly, S.Y., 2018. Tracking Deep Lithospheric Events with Garnet-Websterite Xenoliths from Southeastern Australia. *J. Petrol.* 59, 901–930.
- Mallik, A., Dasgupta, R., 2012. Reaction between MORB-eclogite derived melts and fertile peridotite and generation of ocean island basalts. *Earth Planet. Sci. Lett.* 329–330, 97–108.
- Matson, D.W., Muenow, D.W., Garcia, M.O., 1986. Volatile contents of phlogopite micas from South African kimberlite. *Contrib. Mineral. Petrol.* 93 (3), 399–408.
- Matthey, D., Lowry, D., MacPherson, C., 1994. Oxygen isotope composition of mantle peridotite. *Earth Planet. Sci. Lett.* 128, 231–241.
- McCandless, T.E., Kirkley, M.B., Robinson, D.N., Gurney, J.J., Griffin, W.L., Cousens, D.R., Boyd, F.R., 1989. Some initial observations on polycrystalline diamonds mainly from Orapa. *Ext. Abstr. 28th Int Geological Congress* 47–51.
- Mikhail, S., Howell, D., Hutchison, M.T., Verchovsky, A.B., Warburton, P., Southworth, R., Thompson, A.R., Jones, A.P., Milledge, H.J., 2014a. Constraining the internal variability of the stable isotopes of carbon and nitrogen within mantle diamonds. *Chem. Geol.* 366, 14–23.
- Mikhail, S., Howell, D., McCubbin, F.M., 2014b. Evidence for multiple diamondite forming events in the mantle. *Am. Mineral.* 99, 1537–1543.
- Mikhail, S., Crosby, J.C., Stuart, F.M., Di Nicola, L., Abernethy, F.A.J., 2019a. A secretive mechanical exchange between mantle and crustal volatiles revealed by helium isotopes in 13C-depleted diamonds. *Geochem. Persp. Lett.* 11, 1923.
- Mikhail, S., McCubbin, F.E., Jenner, F.E., Shirey, S.B., Rumble, D., Bowden, R., 2019b. Diamondites: evidence for a distinct tectono thermal diamond forming event beneath the Kaapvaal craton. *Contrib. Mineral. Petrol.* 174, 71–86.
- Mikhail, S., Rinaldi, M., Mare, E.R., Sverjensky, D.A., 2021. A genetic metasomatic link between eclogitic and peridotitic diamond inclusions. *Geochem. Persp. Lett.* 17, 33–38.
- Moore, A., Helmstaedt, H., 2023. Origin of framesite revisited: Possible implications for the formation of CLIPPID diamonds. *Earth Sci. Rev.* 241, 104434.
- Mysen, B.O., Fogel, M.L., Morrill, P.L., Cody, G.D., 2009. Solution behavior of reduced COH volatiles in silicate melts at high pressure and temperature. *Geochim. Cosmochim. Acta* 73 (6), 1696–1710.
- Orlov, J.L., 1977. *The Mineralogy of Diamond*. Wiley, New York.
- Palot, M., Pearson, D.G., Stern, R.A., Stachel, T., Harris, J.W., 2013. Multiple growth events, processes and fluid sources involved in diamond genesis: A micro-analytical study of sulphide-bearing diamonds from Finsch mine. *RSA. Geochim. Cosmochim. Acta* 106, 51–70.
- Petts, D.C., Chacko, T., Stachel, T., Stern, R.A., Heaman, L.M., 2015. A nitrogen isotope fractionation factor between diamond and its parental fluid derived from detailed SIMS analysis of a gem diamond and theoretical calculations. *Chem. Geol.* 410, 188–200.
- Phillips, D., Kiviets, G.B., Barton, E.S., Smith, C.B., Viljoen, F., Fourie, L.F., 1999. ⁴⁰Ar/³⁹Ar dating of kimberlites and related rocks: problems and perspectives, in: Gurney, J.J., Gurney, J.L., Pascoe, M.D., Richardson, S.H. (Eds.), *Proceedings of the VIII International Kimberlite Conference*. Red Roof Design, Cape Town, pp. 677–688.

- Pintér, Z., Foley, S.F., Yaxley, G.M., 2022. Diamonds, dunites, and metasomatic rocks formed by melt/rock reaction in craton roots. *Comm. Earth & Environ.* 3, 296.
- Putnis, A., 2009. Mineral Replacement Reactions. *Rev. Mineral. Geochem.* 70 (1), 87–124.
- Rehfeldt, T., Foley, S.F., Jacob, D.E., Carlson, R.W., Lowry, D., 2008. Contrasting types of metasomatism in dunite, wehrlite and websterite xenoliths from Kimberley, South Africa. *Geochimica et Cosmochimica Acta* 72 (23), 5722–5756.
- Richardson, S.H., Pöml, P.F., Shirey, S.B., Harris, J.W., 2009. Age and origin of peridotitic diamonds from Venetia, Limpopo Belt, Kaapvaal-Zimbabwe craton. *Lithos* 112S, 785–792.
- Rinaldi, M., Mikhail, S., Sverjensky, D.A., Kalita, J., 2023. The importance of carbon to the formation and composition of silicates during mantle metasomatism. *Geochim. Cosmochim. Acta* 356, 105–115.
- Rohrbach, A., Ballhaus, C., Ulmer, P., Golla-Schindler, U., Schönbohm, D., 2011. Experimental evidence for a reduced, metal-saturated upper mantle. *J. Petrol.* 52, 717–731.
- Rosenbaum, J.M., 1993. Mantle phlogopite: a significant lead repository? *Chem. Geol.* 106 (3), 475–483.
- Roskocz, M., Bouhifd, M.A., Jephcoat, A.P., Marty, B., Mysen, B.O., 2013. Nitrogen solubility in molten metal and silicate at high pressure and temperature. *Geochimica et Cosmochimica Acta* 121, 15–28.
- Roskosz, M., Bouhifd, M.A., Jephcoat, A.P., Marty, B., Mysen, B.O., 2013. Nitrogen solubility in molten metal and silicate at high pressure and temperature. *Geochim. Cosmochim. Acta* 121, 15–28.
- Rubanova, E.V., Piazzolo, S., Griffin, W.L., O'Reilly, S.Y., 2012. Deformation microstructures reveal a complex mantle history for polycrystalline diamond. *Geochim. Geophys. Geosys.* 13, Q10010.
- Seggie, A.G., Hannweg, G.W., Colgan, E.A., Smith, C.B., 1999. The geology and geochemistry of the Venetia kimberlite cluster, Northern Province, South Africa, in: Gurney, J.J., Gurney, J.L., Pascoe, M.D., Richardson, S.H. (Eds.), *The P.H. Nixon volume. Red Roof Design, Cape Town*, pp. 750–756.
- Shirey, S.B., Pearson, D.G., Stachel, T., Walter, M.J., 2024. Sublithospheric Diamonds: Plate Tectonics from Earth's Deepest Mantle Samples. *Annu. Rev. Earth Planet. Sci.* 2, 9.1–9.45.
- Shu, C., Foley, S.F., Ezad, I.S., Daczko, N.R., Shcheka, S.S., 2024. Experimental melting of phlogopite websterite in the upper mantle between 1.5 and 4.5 GPa. *J. Petrol.* 65, egae030.
- Smart, K.A., Chacko, T., Stachel, T., Muehlenbachs, K., Stern, R.A., Heaman, L.M., 2011. Diamond growth from oxidized carbon sources beneath the Northern Slave Craton, Canada: a $\delta^{13}\text{C}$ -N study of eclogite-hosted diamonds from the Jericho kimberlite. *Geochim. Cosmochim. Acta* 75, 6027–6047.
- Smelova, G.B., 1994. Origin of Diamond Aggregates from the Kimberlite Pipes of Yakutia (Yakutsk). *Novosibirsk* 87, p in Russian.
- Smith, C.B., 1983. Pb, Sr and Nd isotopic evidence for sources of southern African Cretaceous kimberlites. *Nature* 304, 51–54.
- Smith, E.M., Shirey, S.B., Nestola, F., Bullock, E., Wang, J., Richardson, S.H., Wang, W., 2016. Large gem diamonds from metallic liquid in Earth's deep mantle. *Science* 354, 1403–1405.
- Sobolev, N.V., 1977. Deep-seated inclusions in kimberlites and the problem of the composition of the upper mantle. *AGU, New York*.
- Sobolev, N.V., Lavrentev, Y.G., Pokhilenko, N.P., Usova, L.V., 1973. Chrome-rich garnets from the kimberlites of Yakutia and their parageneses. *Contrib. Mineral. Petrol.* 40, 39–52.
- Sobolev, N.V., Shatsky, V.S., Zedgenizov, D.A., Ragozin, A.L., Reutsky, V.N., 2016. Polycrystalline diamond aggregates from the Mir kimberlite pipe, Yakutia: Evidence for mantle metasomatism. *Lithos* 265, 257–266.
- Stachel, T., 2014. In: *Diamonds in Geology of Gem Deposits*, Mineral Assoc Canada Short Course Ser, pp. 1–28.
- Stachel, T., Harris, J.W., 2008. The origin of cratonic diamonds—Constraints from mineral inclusions. *Ore Geol. Rev.* 34, 5–32.
- Stachel, T., Aulbach, S., Harris, J.W., 2022a. Mineral Inclusions in Lithospheric Diamonds. *Rev. Mineral. Geochem.* 88, 307–391.
- Stachel, T., Cartigny, P., Chacko, T., Pearson, D.G., 2022b. Carbon and nitrogen of mantle-derived diamonds. *Rev. Mineral. Geochem.* 88, 809–876.
- Stern, R.A., Palot, M., Howell, D., Stachel, T., Pearson, D.G., Cartigny, P., Oh, A., 2014. Methods and reference materials for SIMS diamond C- and N-isotope analysis, Canadian Centre for Isotopic Microanalysis, Research Report. University of Alberta Edmonton, Canada.
- Stiefenhofer, J., Viljoen, K.S., Tainton, K.M., Dobbe, R., Hannweg, G.W., 1999. The petrology of a mantle xenolith suite from Venetia, South Africa, in: Gurney, J.J., Gurney, J.L., Pascoe, M.D., Richardson, S.H. (Eds.), *The P.H. Nixon Volume. Red Roof Design, Cape Town*, pp. 836–845.
- Sun, S.-S., McDonough, W.F., 1989. Chemical and isotopic systematics of oceanic basalts: implications for mantle composition and processes, in: Saunders, A.D., Norry, M.J. (Eds.), *Geological Society Special Publication, Magmatism in the Ocean Basins*, pp. 313–345.
- Sunagawa, I., 2005. *Crystals*. Cambridge University Press, Cambridge, New York, Melbourne, Growth, Morphology and Perfection.
- Taylor, W.R., 1990. A reappraisal of the nature of fluids included by diamond - a window in deep-seated mantle fluids and redox conditions. In: Herbert, H.K., Ho, S.E. (Eds.), *Stable Isotopes and Fluid Processes in Mineralization*. University of Western Australia, pp. 333–349.
- Taylor, W.R., Canil, D., Milledge, H.J., 1996. Kinetics of Ib to IaA nitrogen aggregation in diamond. *Geochim. Cosmochim. Acta* 60, 4725–4733.
- Thomassot, E., Cartigny, P., Harris, J.W., Viljoen, K.S., 2007. Methane-related diamond crystallization in the Earth's mantle: Stable isotope evidences from a single diamond-bearing xenolith. *Earth Planet. Sci. Lett.* 257 (3), 362–371.
- Thomson, A.R., Kohn, S.C., Prabhu, A., Walter, M.J., 2021. Evaluating the Formation Pressure of Diamond-Hosted Majoritic Garnets: A Machine Learning Majorite Barometer. *J. Geophys. Res. Solid Earth* 126 (3).
- Tomlinson, E.L., Kamber, B.S., 2021. Depth-dependent peridotite-melt interaction and the origin of variable silica in the cratonic mantle. *Nat. Commun.* 12 (1), 1082.
- Tschauner, O., Huang, S., Greenberg, E., Prakupenka, V., Ma, C., Rossman, G., Shen, A., Zhang, D., Newville, M., Lanzirrotti, A., 2018. Ice-VII inclusions in diamonds: Evidence for aqueous fluid in Earth's deep mantle. *Science* 359 (6380), 1136–1139.
- Vasilev, E., Zedgenizov, D., Zamyatin, D., Klepikov, I., Anonov, A., 2021. Cathodoluminescence of Diamond: Features of Visualization. *Crystals* 11, 1522.
- Viljoen, K.S., Phillips, D., Harris, J.W., Robinson, D.H., 1999. Mineral inclusions in diamonds from the Venetia kimberlites, Northern Province, South Africa. *Proc 7th Int Kimberlite Conf* 2, 888–895.
- Walsh, C., Kamber, B.S., Tomlinson, E.L., 2023. Deep, ultra-hot-melting residues as cradles of mantle diamond. *Nature* 615, 450–454.